JOURNAL OF GEOPHYSICAL RESEARCH, VOL. 108, NO. B1, 2029, doi:10.1029/2001JB001127, 2003

Subduction factory
1. Theoretical mineralogy, densities, seismic wave speeds, and H_2O contents

Bradley R. Hacker
Department of Geological Sciences, University of California, Santa Barbara, California, USA

Geoffrey A. Abers
Department of Earth Sciences, Boston University, Boston, Massachusetts, USA

Simon M. Peacock
Department of Geological Sciences, Arizona State University, Tempe, Arizona, USA

Received 27 August 2001; revised 11 June 2002; accepted 18 July 2002; published 18 January 2003.

[1] We present a new compilation of physical properties of minerals relevant to subduction zones and new phase diagrams for mid-ocean ridge basalt, lherzolite, depleted lherzolite, harzburgite, and serpentinite. We use these data to calculate H_2O content, density and seismic wave speeds of subduction zone rocks. These calculations provide a new basis for evaluating the subduction factory, including (1) the presence of hydrous phases and the distribution of H_2O within a subduction zone; (2) the densification of the subducting slab and resultant effects on measured gravity and slab shape; and (3) the variations in seismic wave speeds resulting from thermal and metamorphic processes at depth. In considering specific examples, we find that for ocean basins worldwide the lower oceanic crust is partially hydrated (<1.3 wt % H_2O), and the uppermost mantle ranges from unhydrated to ~20% serpentinized (~2.4 wt % H_2O). Anhydrous eclogite cannot be distinguished from harzburgite on the basis of wave speeds, but its ~6% greater density may render it detectable through gravity measurements. Subducted hydrous crust in cold slabs can persist to several gigapascals at seismic velocities that are several percent slower than the surrounding mantle. Seismic velocities and V_P/V_S ratios indicate that mantle wedges locally reach 60–80% hydration. *INDEX TERMS:* 3040 Marine Geology and Geophysics: Plate tectonics (8150, 8155, 8157, 8158); 3660 Mineralogy and Petrology: Metamorphic petrology; 3919 Mineral Physics: Equations of state; 5199 Physical Properties of Rocks: General or miscellaneous; 8123 Tectonophysics: Dynamics, seismotectonics; *KEYWORDS:* subduction, seismic velocities, mineral physics, H_2O

Citation: Hacker, B. R., G. A. Abers, and S. M. Peacock, Subduction factory, 1, Theoretical mineralogy, densities, seismic wave speeds, and H_2O contents, *J. Geophys. Res.*, *108*(B1), 2029, doi:10.1029/2001JB001127, 2003.

1. Introduction

[2] A consistent thermal-petrological-seismological model of subduction zones could be a powerful tool to further our understanding of the subduction process. Even if such a model were incomplete, it might still be a useful means of contrasting one subduction zone against another or for comparing subducted versus unsubducted lithosphere. This paper is our attempt to build a consistent model; the companion paper [*Hacker et al.*, 2003], on the relationship between intermediate-depth seismicity and metamorphism, gives an example of how such a model can be used. Our approach comprises six specific steps:

1. Compile and assess physical properties of minerals relevant to subduction zones.
2. Construct phase diagrams appropriate for subduction zone rock types and physical conditions.
3. Compute pressures (P) and temperatures (T) for a specific subduction zone.
4. Superimpose calculated phase relations onto the P–T model.
5. Superimpose rock physical properties onto the P–T model.
6. Compare predictions to observations.

0148-0227/03/2001JB001127$09.00

2. Compiling Mineral Properties

[3] We performed an extensive literature search to obtain physical properties of minerals relevant to subduction zones. To estimate densities and seismic velocities at elevated P and T, the physical properties that are needed, and known to

Table 1. Physical Properties of Subduction Zone Minerals[a]

Phase	Gram Formula Weight, g/mol	Molar Volume, cm^3/mol	ρ_{298}, kg/m^3	Notes and Refs	H_2O, wt %	Expansivity a_o, $\times 10^5\ K^{-1}$	Notes and Refs	K_T, $\times 10^{10}$ Pa	Notes and Refs	$K'_T = \partial K_T/\partial P$	Notes and Refs	μ, $\times 10^{10}$ Pa	Notes and Refs	$\Gamma = (\partial \ln\mu/\partial \ln\rho)_P$	Notes and Refs	$\mu' = \partial\mu/\partial P$	Notes and Refs	γ_{th}	Notes and Refs	δ_T	Notes and Refs
hab, high albite	262.2	100.1	2620	[21]	0	4.6	[19]	5.4	D94	6	D94	2.8	[9]	13	[14]	4.26	H96	0.6	[20]	6.58	[18]
lab, low albite	262.2	100.1	2620	[21]	0	4.6	[19]	5.4	D94	6	D94	2.8	[9]	13	[16]	4.26	[17]	0.6	[20]	6.57	[18]
an, anorthite	278.2	100.8	2760	[21]	0	2.4	[19]	8.4	A01	3.0	Apc	3.7	[9]	6.8	[14]	3.48	H96	0.5	[20]	3.47	[18]
alm, almandine	497.7	115.1	4324	[21]	0	4.0	[19]	17.4	WJ01	6.0	WJ01	9.21	WJ01	5.5	[16]	1.6	H96	1.0	[20]	5.52	H96
grs, grossular	450.4	125.4	3593	[21]	0	3.9	[19]	16.8	WJ01	5.5	WJ01	10.9	WJ01	5.1	[14]	1.2	H96	1.2	AI95	4.57	AI95
prp, pyrope	403.1	113.1	3565	[21]	0	4.4	[19]	17.3	WJ01	5.0	WJ01	9.10	WJ01	4.1	[14]	1.5	SB01	1.3	AI95	5.30	AI95
di, diopside	216.6	66.2	3272	[21]	0	5.7	[19]	11.3	K95	4.8	K95	6.49	B95	6.0	[16]	2.00	H96	1.2	[20]	6.04	[18]
en, enstatite	200.8	62.6	3206	[21]	0	5.1	[19]	10.6	A01	8.5	A01	7.68	J99	9.4	[16]	2.00	H96	0.9	[20]	9.39	[18]
fs, ferrosilite	263.9	65.9	4003	[21]	0	6.3	[19]	10.0	[15]	4	[13]	5.20	B95	5.1	[16]	2.00	H96	1.1	[20]	5.05	[18]
jd, jadeite	202.1	60.4	3346	[21]	0	4.7	[19]	13.9	K95	4	[13]	8.50	B95	5.0	[16]	1.02	H96	1.0	[20]	4.99	[18]
hed, hedenbergite	248.1	68.0	3651	[21]	0	5.7	[19]	11.9	K95	4	[13]	6.1	B95	5.2	[16]	0.85	[17]	1.2	[20]	5.21	[18]
clin, clinochlore	555.6	210.8	2635	[21]	13	4.0	[19]	7.54	WM01	4	HF78	4.55	[7]	4.3	[16]	1.00	[17]	0.3	[20]	4.30	[18]
daph, daphnite	713.5	213.4	3343	[21]	10.1	4.0	[19]	4.58	HF78	4	[13]	2.76	[7]	4.3	[16]	1.00	[17]	0.3	[20]	4.29	[18]
law, lawsonite	314.2	101.3	3101	[21]	11.5	3.2	C00	12.3	BA01	5.4	BA01	6.02	L80	6.3	[16]	0.82	[17]	0.9	[20]	6.25	[18]
gl, glaucophane	789.4	262.4	3008	[21]	2.3	5.3	[19]	9.6	C91	4	C91	5.6	[10]	4.8	[16]	0.97	[17]	0.8	[20]	4.81	[18]
fgl, ferroglaucophane	878.1	265.9	3302	[21]	2.1	5.3	[19]	8.9	HP98	4	[13]	5.2	[10]	4.8	[16]	0.97	[17]	0.8	[20]	4.81	[18]
tr, tremolite	812.4	272.7	2979	[21]	2.2	5.3	[19]	8.5	C91	4	C91	4.9	[10]	4.7	[16]	0.97	[17]	0.7	[20]	4.74	[18]
fact, ferro-actinolite	970.1	282.8	3430	[21]	1.9	5.3	[19]	7.6	HP98	4	[13]	4.4	[10]	4.7	[16]	0.97	[17]	0.7	[20]	4.73	[18]
ts, tschermakite	815.4	268.0	3043	[21]	2.2	5.3	[19]	7.6	HP98	4	[13]	4.4	[10]	4.7	[16]	0.97	[17]	0.7	[20]	4.71	[18]
parg, pargasite	835.8	271.9	3074	[21]	2.2	5.3	[19]	9.12	HP98	4	[13]	5.29	[10]	4.8	[16]	0.97	[17]	0.8	[20]	4.84	[18]
hb, hornblende	864.7	266.2	3248	[8]	2.5	5.3	[19]	9.40	[8]	4	C91	5.45	[3]	5.1	[16]	0.97	[17]	1.1	[13]	5.10	[18]
anth, anthophyllite	780.8	265.4	2942	[21]	2.3	5.3	[19]	7.0	HP98	4	[13]	4.1	[10]	4.6	[16]	0.97	[17]	0.6	[20]	4.60	[18]
pr, prehnite	412.4	140.3	2940	[21]	4.4	5.1	[19]	8.35	HP98	4	[13]	5.03	[7]	4.8	[16]	1.00	[17]	0.8	[20]	4.77	[18]
pm, pumpellyite	943	295.5	3191	[21]	6.7	5.0	[19]	16.2	HP98	4	[13]	7.91	L80	5.3	[16]	0.82	[17]	1.3	[20]	5.30	[18]
aqz, alpha quartz	60.1	22.7	2648	[21]	0	0.65	[19]	3.71	A97	5.99	A97	4.48	O95	40.1	[14]	0.46	B95	0.7	[20]	8.42	H96
bqz, beta quartz	60.1	23.7	2530	[21]	0	0.65	[19]	5.70	[15]	4	[13]	4.14	B95	4.1	[16]	1.21	[17]	0.1	[20]	4.11	[18]
coe, coesite	60.1	20.6	2911	[21]	0	1.8	[19]	9.74	A01	4.3	A01	6.16	B95	4.7	[16]	1.05	[17]	0.4	[20]	4.66	[18]
zo, zoisite	454.4	135.8	3347	[21]	2	6.7	[19]	12.5	G00	4	G00	6.12	H96	5.2	[16]	0.82	[17]	1.2	[20]	5.24	[18]
czo, clinozoisite	454.4	136.3	3333	[21]	2	4.6	[19]	12.5	[22]	5	[22]	6.12	L80	5.9	[16]	0.82	[17]	0.9	[20]	5.94	[18]
ep, epidote	483.2	138.1	3498	[21]	1.9	5.1	[19]	16.2	[15]	4	[13]	6.12	B95	5.1	[16]	0.63	[17]	1.1	[20]	5.11	[18]
ms, muscovite	398.2	140.8	2828	[21]	4.5	6.0	[19]	6.14	K95	6.9	K95	3.70	[3]	7.4	[16]	1.00	[17]	0.5	[20]	7.42	[18]
phl, phlogopite	417.2	149.7	2788	[21]	4.5	5.8	[19]	5.85	HF78	4	HF78	2.70	[3]	4.6	[16]	0.77	[17]	0.6	[20]	4.55	[18]
ann, annite	511.9	154.3	3317	[21]	3.5	5.8	[19]	5.04	[4]	4	[13]	2.66	[4]	4.6	[16]	0.88	[17]	0.6	[20]	4.55	[18]
atg, antigorite	4536	1754.7	2585	[21]	12.3	4.7	[19]	6.35	T91	2.77	T91	1.81	[1]	3.3	[16]	0.47	[17]	0.5	T91	3.28	[18]
fo, forsterite	140.7	43.7	3222	[21]	0	6.1	[19]	12.7	AI95	5.37	AI95	8.16	AI95	5.2	[14]	1.82	AI95	1.2	AI95	5.50	AI95
fa, fayalite	203.8	46.3	4400	[21]	0	5.1	[19]	13.7	AI95	5.16	AI95	5.10	AI95	4.7	[14]	0.62	AI95	1.1	AI95	5.40	AI95
cc, calcite	100.1	36.9	2713	[21]	0	4.4	[19]	7.35	RA99	4	RA99	3.20	B95	4.7	[16]	0.73	[17]	0.7	[20]	4.69	[18]
ar, aragonite	100.1	34.1	2931	[21]	0	12	[19]	4.60	[15]	4	[13]	3.85	B95	5.4	[16]	1.39	[17]	1.4	[20]	5.36	[18]
lm, laumontite	470.4	203.7	2309	[21]	15.3	2.4	[19]	4.66	C96	4	[13]	2.80	C96	4.5	[16]	1.00	[17]	0.5	[20]	4.46	[18]
wr, wairakite	434.4	190.5	2281	[21]	8.3	2.4	[19]	4.66	C96	4	[13]	2.80	C96	4.5	[16]	1.00	[17]	0.5	[20]	4.52	[18]
br, brucite	58.3	24.6	2368	[21]	30.9	13	PW96	3.96	X98	6.7	X98	2.39	[7]	4.5	[16]	1.00	[17]	0.8	[20]	4.5	F95
ta, talc	379.7	136.4	2784	[21]	4.8	3.7	[19]	4.16	P95	6.5	P95	2.26	BH00	6.8	[16]	0.91	[17]	0.3	[20]	6.82	[18]
chum, chlinohumite	621.1	197.4	3146	[21]	2.9	5.0	[19]	12.0	HP98	4	[13]	7.69	[6]	4.9	[16]	1.07	[17]	0.9	[20]	4.91	[18]
phA, phase A	456.3	154.4	2955	[21]	11.8	8.3	PW96	9.74	RC00	6.0	RC00	6.24	[6]	7.8	[16]	1.07	[17]	1.8	[20]	7.79	[18]
sil, sillimanite	162.0	49.9	3249	[21]	0	2.2	[19]	17.1	[15]	4	[13]	9.15	B95	4.5	[16]	0.89	[17]	0.5	[20]	4.50	[18]

Table 1. (continued)

Phase	Gram Formula Weight, g/mol	Molar Volume, cm^3/mol	ρ_{298}, kg/m^3	Notes and Refs	H_2O, wt %	Expansivity a_o, $\times 10^5\ K^{-1}$	Notes and Refs	K_T, $\times 10^{10}$ Pa	Notes and Refs	$K_T' = \partial K_T/\partial P$	Notes and Refs	μ, $\times 10^{10}$ Pa	Notes and Refs	$\Gamma = (\partial \ln\mu/\partial \ln\rho)_P$	Notes and Refs	$\mu' = \partial\mu/\partial P$	Notes and Refs	γ_{th}	Notes and Refs	δ_T	Notes and Refs
ky, kyanite	162.0	44.1	3670	[21]	0	4.0	[19]	15.6	C97	5.6	C97	8.37	[11]	6.6	[16]	0.89	[17]	1.0	[20]	6.56	[18]
or, orthoclase	278.3	108.9	2555	[21]	0	3.4	[19]	5.83	AA97	4	AA97	2.81	B95	4.4	[16]	0.80	[17]	0.4	[20]	4.44	[18]
san, sanidine	278.3	109.0	2553	[21]	0	3.4	[19]	6.70	A88	4	A88	3.23	[12]	4.4	[16]	0.80	[17]	0.4	[20]	4.44	[18]
spl, spinel	142.3	39.8	3575	[21]	0	4.3	[19]	20.8	AI95	3.36	AI95	10.8	AI95	4.2	[14]	0.87	[17]	1.3	A195	6.5	A195
herc, hercynite	173.8	40.8	4264	[21]	0	4.0	[19]	20.9	[15]	4	[13]	8.45	B95	5.2	[16]	0.67	[17]	1.2	[20]	5.19	[18]
magn, magnetite	231.5	44.5	5201	[21]	0	7.0	[19]	18.1	K95	5.5	K95	10.2	[3]	7.5	[16]	0.94	[17]	2.0	[20]	7.45	[18]

[a]Values are from *Holland and Powell* [1998], except Apc: R. Angel (personal communication, 1999); A88, *Angel et al.* [1988]; AI95, *Anderson and Isaak* [1995]; B95, *Bass* [1995]; BH00, [*Bailey and Holloway*, 2000]; C82, *Christensen* [1982]; C91, *Comodi et al.* [1991]; C96, *Christensen* [1996]; C97, *Comodi et al.* [1997]; C00, *Chimmey et al.* [2000]; F95, *Fei* [1995]; G00, *Grevel et al.* [2000]; H96, *Helffrich* [1996]; HF78, *Hazen and Finger* [1978]; HP98, *Holland and Powell* [1998]; J99, *Jackson et al.* [1999]; K95, *Knittle* [1995]; L80, *Levien et al.* [1980]; O95, *Ohno* [1995]; P95, *Pawley et al.* [1995]; PW96, *Pawley and Wood* [1996]; RA99, *Redfern and Angel* [1999]; SB01, *Sinogeikin and Bass* [2000, #3653]; T91, *Tyburczy* [1991]; W101, *Wang and Ji* [2001]; WM01, *Welch and Marshall* [2001]. Notes [1], adjusted to fit STP Poisson's ratio measured by *Tyburczy* [1991]; [2], assumed; [3], adjusted to fit STP Poisson's ratio from *Christensen* [1982, 1996]; [4], calculated using "phlogopite" and "biotite" properties given by *Christensen* [1982] and extrapolating on the basis of densities of *Holland and Powell* [1998]; [5], calculated from *Bass* [1995] by regression of other measured garnet compositions; [6], calculated using Poisson's ratio for forsterite and scaled against bulk modulus of forsterite (structures are similar); [7], calculated using Poisson's ratio for muscovite and scaled against bulk modulus of muscovite (all are phyllosilicates); [8], we chose hornblendite data [*Christensen*, 1996] over hornblende data [*Alexandrov and Ryzhova*, 1961]; [9], calculated from regression fit to intermediate-composition plagioclase Poisson's ratios of *Ryzhova* [1964]; [10], calculated using Poisson's ratio for hornblende and scaled against bulk modulus of hornblende (structures are similar); [11], calculated using Poisson's ratio for sillimanite and scaled against bulk modulus of sillimanite (structures are similar); [12], calculated using Poisson's ratio for orthoclase and scaled against bulk modulus of orthoclase (structures are similar); [13], assumed, common value [*Anderson*, 1989]; [14], calculated at high T using *Anderson and Isaak*'s [1995] highest temperatures, where $d\mu/dT$ is nearly constant; [15], adjusted from *Bass* [1995], using $K_T = K_S/(1 + \alpha\gamma_{th}T)$ [*Anderson et al.*, 1992]; [16], approximated as $\Gamma \approx \delta_T$ [*Anderson et al.*, 1992]; [17], approximated as $\mu' \approx 5/3/\mu/K_T$ [*Anderson et al.*, 1992]; [18], approximated as $\delta_T \approx \gamma_{th} + K_T'$ [*Anderson et al.*, 1992]; [19], we used *Holland and Powell*'s [1998] values and expansion for thermal expansivity: $a(T) = a^o(1-10*\mathrm{sqrt}(T))$, giving $\ln(V(T)/V_o) = a^o*[(T - 298 + \mathrm{sqrt}(T) - \mathrm{sqrt}(298)$; [20], γ_{th} was calculated using *Bina and Helffrichs'* [1992] equation 16 at 1000 K, using *Holland and Powell*'s [1998] values and $\delta = 4$; [21], mass, density, and H_2O content were calculated from mineral formula of *Holland and Powell* [1998]; [22], we used zoisite K_T and K_T' for clinozoisite, following *Grevel et al.* [2000].

sufficient degree [e.g., *Anderson et al.*, 1992; *Bina and Helffrich*, 1992], include formula weight, molar volume, H_2O content, expansivity α, $\partial\alpha/\partial T$, isothermal bulk modulus K_T, $\partial K_T/\partial P$, shear modulus μ, $\partial\mu/\partial P$, $\Gamma = (\partial \ln\mu/\partial \ln\rho)_P$, Grüneisen parameter γ_{th}, and second Grüneisen parameter $\delta_T = (\partial \ln K_T/\partial \ln\rho)_P$ (Table 1). From these, we calculated the adiabatic bulk modulus, shear modulus, density, seismic wave speeds, and Poisson's ratios for each mineral as a function of P and T, following *Bina and Helffrich* [1992], ignoring the second pressure derivatives of the moduli, but (1) describing the dependence of $\mu(T)$ via Γ [*Anderson et al.*, 1992], and (2) using *Holland and Powell*'s [1998] approximation for α(T) (see Appendix A). Each of these calculated values was examined in detail to ensure agreement with values measured directly on minerals or monomineralic aggregates at elevated P and T, as summarized elsewhere [e.g., *Christensen*, 1996]. Major deficiencies in this dataset, most notably in the paucity of μ and $\partial\mu/\partial T$ values, should provide an impetus for mineral physicists to conduct further work.

3. Constructing Phase Diagrams

[4] We chose to model only a restricted set of the most abundant rock compositions relevant to subduction zones: basalt/gabbro, lherzolite, depleted lherzolite, harzburgite, and serpentinite. We treated the entire crust of the overriding and subducting plates as basalt and gabbro of mid-ocean ridge basalt (MORB) composition, and the entire mantle as ultramafic. For each rock composition, we calculated the P–T stability fields of different minerals and the reactions that bound the various fields. We treated each stability field as though it contained a single set of minerals of constant composition and mode, and as though it were bounded by discontinuous reactions. This is a more serious simplification for mafic rocks than for ultramafic rocks.

3.1. Mafic Rocks

[5] There are many different ways to construct a phase diagram for mafic rocks. One internally consistent approach, taken by *Kerrick and Connolly* [2001], is to specify the bulk composition in terms of major elements and then calculate phase assemblages based on minimizing Gibbs free energy. A weakness of this approach is the heavy reliance on the thermodynamic properties of minerals, which are known to varying degrees of accuracy and precision. A second approach is to use experimental observations of the stabilities of minerals. The strength of this methodology is that important variables such as pressure, temperature, and bulk composition are specified by the experimentalist. A crucial weakness of using experiments is that it is nearly impossible to reverse reactions at low temperature (typically <600°C), and many experiments conducted at such conditions have yielded metastable minerals.

[6] We used a third approach, which involved a comprehensive search of the literature to identify petrological field studies that reported bulk rock compositions, mineral modes, and mineral compositions. From these studies we chose only those rocks with bulk compositions that differed from unmetasomatized, anhydrous MORB (Table 2) by less than ~10% in each oxide. We then compiled the mineral modes and mineral compositions into various metamorphic facies (Table 3). Obvious outliers were discarded, and a

Table 2. Mid-ocean Ridge Basalt Compositions[a]

	Unaltered[b]	Altered[c]
SiO_2	50.6	48.9
Al_2O_3	15.7	16.6
TiO_2	1.5	1.3
FeO*	10.6	9.6
MgO	7.6	7.1
CaO	11.1	13.7
Na_2O	2.6	2.2
K_2O	0.2	0.6

[a]Units in weight percent.

[b]Unaltered MORB, anhydrous, 8 major oxides [*Pearce*, 1976; *Wilson*, 1989].

[c]Altered MORB, anhydrous, 8 major oxides [*Staudigal et al.*, 1996].

mean mineral mode and set of mean mineral compositions were computed for each metamorphic facies. Each mineral composition was then decomposed proportionally into end-member phases listed in Table 1 (e.g., garnets are represented as mixtures of almandine, grossular, and pyrope end-members). Because many natural mineral compositions are not easily decomposed into constituent components for which we have physical property data (e.g., ferric-iron or Ti-bearing amphibole) each mineral mode was adjusted, using rules given in Table 4, to ensure that the bulk composition calculated from the modes and compositions of the end-member mineral components was still within 10% of MORB. The H_2O content of each rock thus calculated was not fixed or limited, but determined by the mineral modes. Note that even the least hydrous rocks we calculated for MORB composition contain a tiny fraction of H_2O bound in mica.

[7] Next, the stoichiometries and P–T positions of the reactions that were judged to bound the various mineral assemblages were calculated with the aid of Thermocalc [*Powell et al.*, 1998] in the system K-Na-Ca-Mg-Fe^{2+}-Fe^{3+}-Al-Si-O-H. Most facies boundaries are thus defined by the appearance or disappearance of at least one phase, in addition to changes in the compositions and modes of minerals with solid solutions. The result is shown in Figure 1. Several important observations apply to Figure 1.

1. Metamafic rocks have never been recovered from extremely low temperatures (i.e., the ''forbidden zone'' of *Liou et al.* [2000]), so phase relations in this domain are speculative. However, we calculate assemblages in the forbidden zone because calculated geotherms for cold subduction zones penetrate into this region [*Peacock and Wang*, 1999].

Table 3. Mineral Modes for MORB at Various Metamorphic Facies[a]

	Basalt	Gabbro	Z	PP	PA	GS	eA	gA	egA	A	G	gG
hab, high albite											21	
lab, low albite	16	10	19	20	21	22	20	11	11	18		20
an, anorthite	38	38						6		18	21	15
alm, almandine								11	7			5
grs, grossular								8	3			13
prp, pyrope								3	1			10
di, diopside	28	26									5	5
en, enstatite		5									9	9
fs, ferrosilite		6									9	9
jd, jadeite												2
hed, hedenbergite	9	6									9	11
clin, clinochlore			18	16	11	11	2		4			
daph, daphnite			10	8	6	8	3		3			
law, lawsonite					4							
gl, glaucophane									7			
fgl, ferroglaucophane								17	6			
tr, tremolite					8	12	9	18	5	13	2	
fact, ferro-actinolite					14	5	16	5	3	25	7	
ts, tschermakite							15	14		12	9	
parg, pargasite							10			12	7	
pr, prehnite				14								
pm, pumpellyite				13	18							
qz, quartz			8	13	5	5	2	2	5	1		
coe, coesite												
zo, zoisite								4				
czo, clinozoisite												
ep, epidote					8	32	18		20			
ms, muscovite			2	2	2	2	2		15			
phl, phlogopite									2			
fo, forsterite	1	7										
fa, fayalite		2										
cc, calcite			12	5					4			
lm, laumontite			25									

[a]In units of volume percent. Mineral abbreviations from *Holland and Powell* [1998]. Z, zeolite; PP, prehnite-pumpellyite; PA, prehnite-actinolite; GS, greenschist; eA, epidote amphibolite; gA, garnet amphibolite; egA, epidote-garnet amphibolite; A, amphibolite; G, granulite; gG, garnet granulite; lB, lawsonite blueschist; jlB, jadeite-lawsonite blueschist; cjlB, coesite-jadeite-lawsonite blueschist; jltS, jadeite-lawsonite-talc schist; eB, epidote blueschist; jeB, jadeite-epidote blueschist; zaE, zoisite-amphibole eclogite; aE, amphibole eclogite; zE, zoisite eclogite; laE, lawsonite-amphibole eclogite; E, eclogite; cE, coesite eclogite; dE, diamond eclogite. References used to compile this table are *Boyle* [1986], *Coleman et al.* [1965], *Cotkin* [1987], *Davies and Warren* [1992], *El-Shazly* [1994], *El-Shazly et al.* [1990], *El-Shazly et al.* [1997], *Erdmer and Helmstaedt* [1983], *Ernst* [1977], *Evans et al.* [1981], *Evans et al.* [1979], *Glassley and Sørensen* [1980], *Godard* [1988], *Laird and Albee* [1981], *Liou et al.* [1975], *Maresch and Abraham* [1981], *Moore* [1986], *Morgan* [1970], *Okay* [1980b, 1980a], *Okay* [1995], *Preto* [1970], *Reid et al.* [1976], *Stephenson and Hensel* [1982], and *Thelin et al.* [1990].

Table 4. Rules for Decomposing Natural Rock/Mineral Compositions Into End-Member Minerals

Rock/Mineral	Composition
Greenschist and related facies	all Na in albite; all K in muscovite; all Ti in sphene; epidote assumed to have $Fe^{3+}/(Fe^{3+} + Al) = 0.33$; remaining mineral modes adjusted to fit MORB bulk composition while preserving mineral Fe/Mg ratios
Amphibolite, granulite, and related facies	all Na in albite + pargasite; all K and Ti in hornblende; assumed 1 vol % magnetite; assumed An_{50} plagioclase; epidote assumed to have $Fe^{3+}/(Fe^{3+} + Al) = 0.33$; remaining mineral modes adjusted to fit MORB bulk composition while preserving mineral Fe/Mg ratios.
Garnet-amphibolite facies	all Na in albite + ferroglaucophane; all K in hornblende; all Ti in rutile; assumed An_{35} plagioclase; remaining mineral modes adjusted to fit MORB bulk composition while preserving mineral Fe/Mg ratios
Various blueschist facies	all Na in albite + glaucophane + ferroglaucophane; all K in muscovite; all Ti in sphene; remaining mineral modes adjusted to fit MORB bulk composition while preserving mineral Fe/Mg ratios
Various eclogite facies	all Na in jadeite; all K in muscovite; all Ti in sphene; zoisite assumed to have $Fe^{3+} = 0$; remaining mineral modes adjusted to fit MORB bulk composition while preserving mineral Fe/Mg ratios

2. Our phase diagram is consistent with mineralogies of high-pressure to ultrahigh-pressure rocks; for example, in the ultrahigh-pressure Kokchetav Massif, quartz eclogites contain zoisite and amphibole, coesite eclogites contain rare amphibole, and diamond eclogites contain neither zoisite nor amphibole [*Ota et al.*, 2000].

3. There is no stability field for chloritoid in Figure 1, consistent with its absence in naturally metamorphosed rocks of MORB composition (but see *Poli and Schmidt* [1997]).

4. The restricted phase field for lawsonite eclogites is consistent with the extreme rarity of such rocks, but see *Okamoto and Maruyama* [1999] for a different interpretation. Specifically, lawsonite eclogites have been reported in mafic bulk compositions from three localities. In one of those [*Helmstaedt and Schulze*, 1988], lawsonite may not be an eclogite-facies phase. In another locality (Corsica), lawsonite occurs in unusually Fe + Mn-rich eclogites [*Caron and Pequignot*, 1986]. The third locality is a single boulder [*Ghent et al.*, 1993].

Table 3. (continued)

	Basalt	Gabbro	Z	PP	PA	GS	eA	gA	egA	A	G	gG	
ta, talc													
sphene + rutile + spinel			2	3	3	3	3	1	2				
mt, magnetite	8		4	6					2	1	1	1	
	lB	jlB	cjlB	jltS	eB	jeB	zaE	aE	zE	laE	E	cE	dE
hab, high albite													
lab, low albite	10				18								
an, anorthite													
alm, almandine							17	17	18	8	18	18	19
grs, grossular							7	15	8	7	13	13	14
prp, pyrope							8	7	8	4	11	11	12
di, diopside							11	15	20	7	24	24	21
en, enstatite									4				1
fs, ferrosilite				3			1		2		4	4	3
jd, jadeite		8	8	16		13	13	12	17	10	18	18	18
hed, hedenbergite				21			2	3	5	1	2	2	5
clin, clinochlore	4	5	5	5	8	8				3			
daph, daphnite	5	4	4	4	8	8				2			
law, lawsonite	27	28	28	28						14			
gl, glaucophane	7	11	11		4	4	1			5			
fgl, ferroglaucophane	9	6	6		4	4	5	10		8			
tr, tremolite	17	14	14		15	15	10	4		9			
fact, ferro-actinolite	13	17	17		5	5	1	2		10			
ts, tschermakite							3						
parg, pargasite								8		4			
pr, prehnite													
pm, pumpellyite													
qz, quartz	3	2		2	5	10	7	3	6	3	6		
coe, coesite			2									6	3
zo, zoisite							10		8				
czo, clinozoisite					5	5							
ep, epidote					23	23							
ms, muscovite	2	2	2	2	2	2	2	2	2	2	2	2	2
phl, phlogopite													
fo, forsterite													
fa, fayalite													
cc, calcite													
lm, laumontite													
ta, talc				16									
sphene + rutile + spinel	3	3	3	3	3	3	2	2	2	3	2	2	2
mt, magnetite													

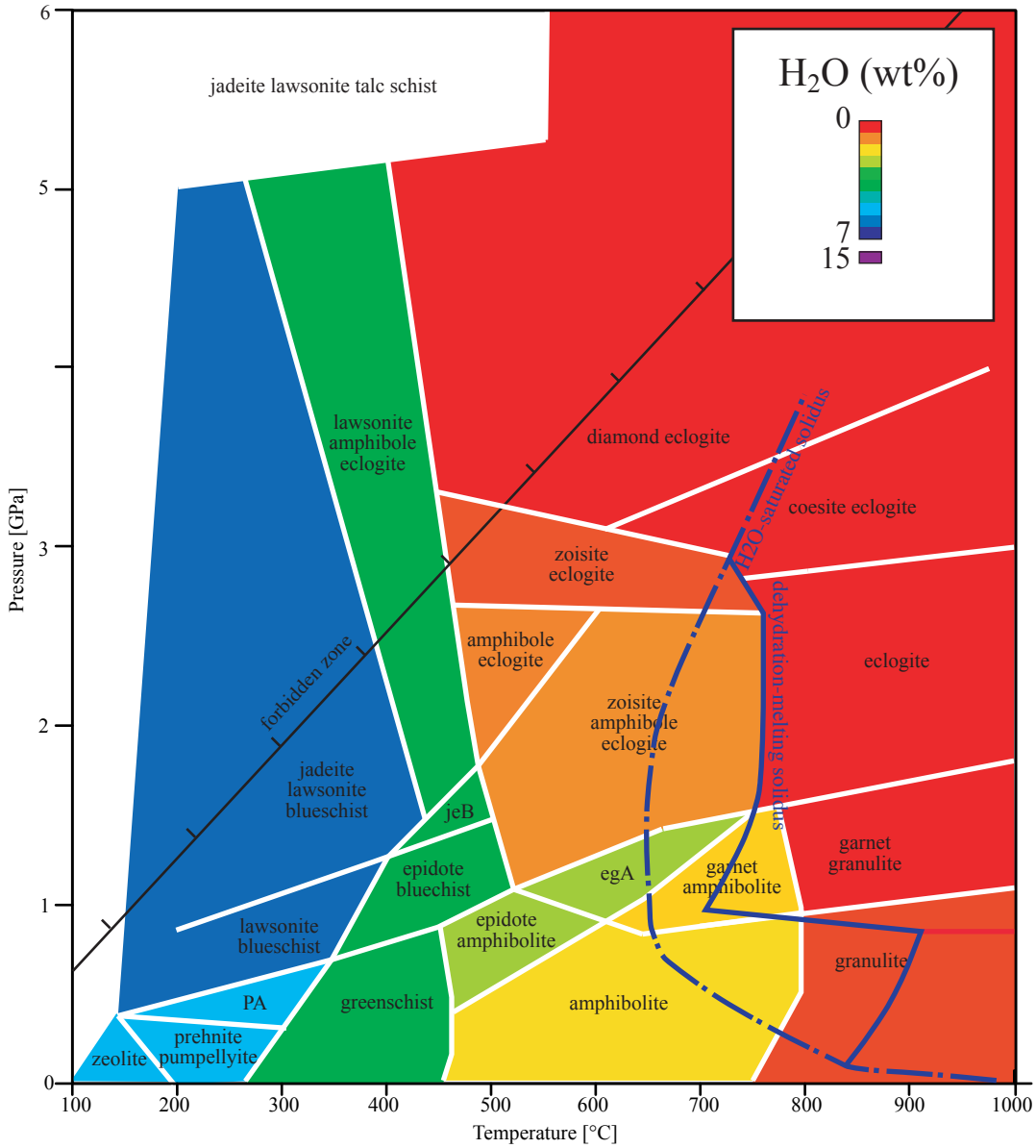

Figure 1. Phase diagram for MORB; abbreviations as in Table 3. Phase relations in the íí forbidden zone (PT conditions not represented by rocks exposed on Earth s surface [Liou et al., 2000]) are poorly known. Solidi and high-pressure phase relations modified per results of Vielzeuf and Schmidt [2001].

Figure 2. (opposite) Phase diagram for lherzolite. Mineral abbreviations are after Holland and Powell [1998], plus am, amphibole; chl, chlorite; cpx, clinopyroxene, excluding CaTs (Ca tschermak); gar, garnet; ol, olivine; opx, orthopyroxene, excluding MgTs. Mineralogy of each field shown as m%, modal percentage of each mineral; v%, vol % of each mineral; m, moles of each mineral relative to the unaltered íí starting composition. Phase relations at T < 600□C, P > 5 GPa poorly known. Reactions show stoichiometry appropriate for the starting composition. Line weights are proportional to □H_2O, and show that the H_2O is lost between □500 and 800□C. Additional reactions are [1] 6en + 6di + 6sp = 12fo + 6an; [2] 12en + 6sp = 6py + 6fo; [3] 1.5 di + 1.5py = 1.5cats + 3en; [4] 2py = 2en + 2mgts; [5] 2en + 2sp = 2fo + 2mgts; [6] 3.8fo + 3.8tr = 9.4en + 7.5di + 2H_2O; [7] 6.8fo + 6.8tr = 16.9en + 13.5di + 6.8H_2O; [8] 1.5di + 1.5sp = 1.5fo + 1.5cats; [9] 3tr + 6sp = 1.5en + 9fo + 6an + 3H_2O; [10] 3.5clin = 3.5en + 3.5fo + 3.5sp + 14H_2O; [11] 0.4clin + 0.2tr = 2.2fo + 1.1en + 0.9an + 4H_2O; [12] 5.1di + 5.1clin = 15.3fo + 5.1an + 20H_2O; [13] 3.1clin = 3.1en + 3.1fo + 3.1sp + 12.4H_2O; [14] 6.4clin + 5.1di = 9fo + 2.6tr + 6.4sp + 23H_2O; [15] 9.5clin = 9.5en + 9.5fo + 9.5sp + 38H_2O; [16] 4.2fo + 4.2tr = 10.5en + 8.4di + 4.2H_2O; [17] 19en + 9.5sp = 9.5py + 9.5fo.

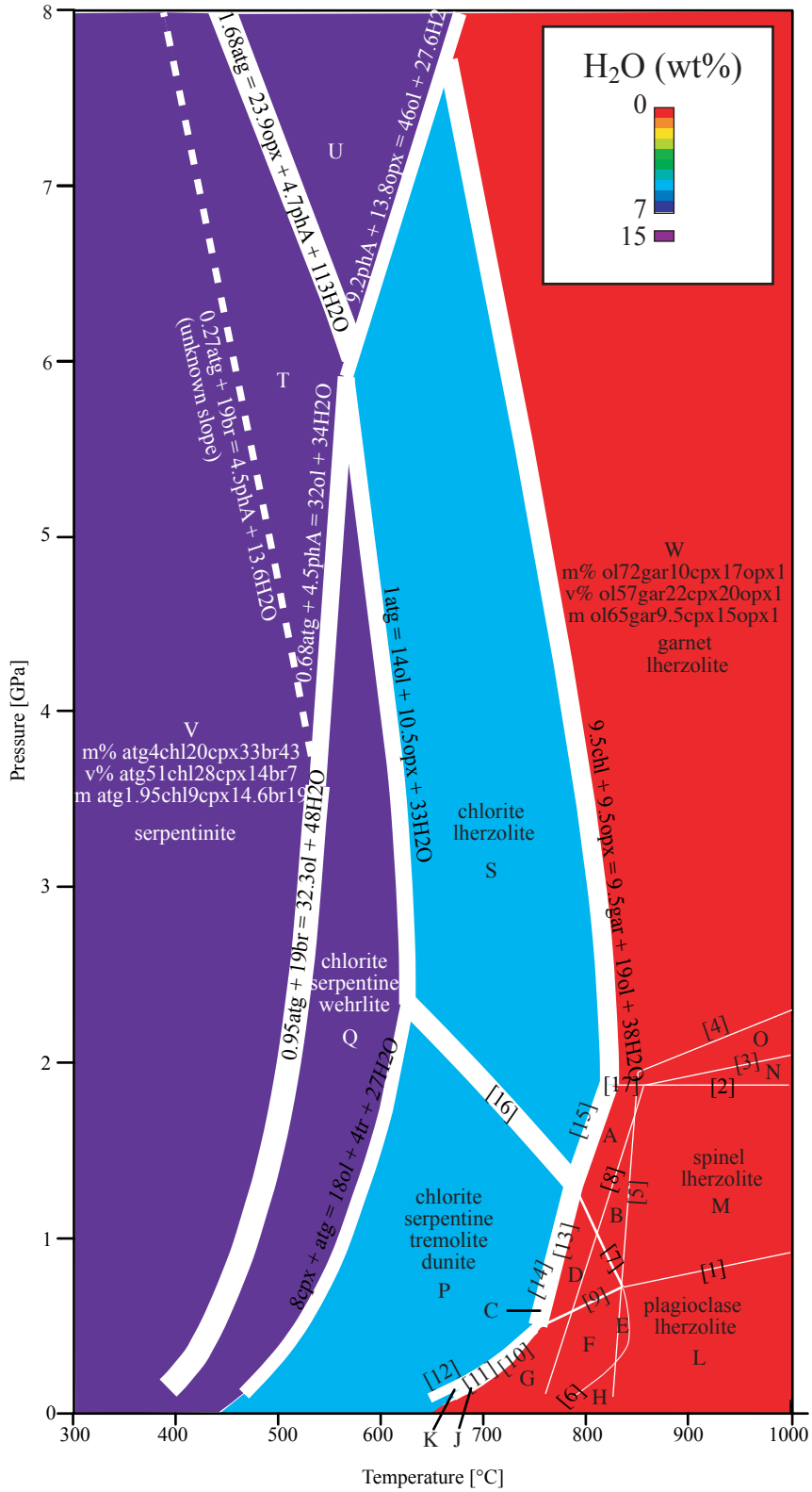

A (0 wt% H_2O)
m% ol56opx20cpx15sp10
v% ol48opx25cpx20sp7
m ol55.5opx20cpx15sp9.5

B (0 wt% H_2O)
m% ol57opx20cpx15sp8
v% ol48opx25cpx20sp6
m ol57opx20(cpx13.5cats1.5)sp8

C (2.3 wt% H_2O)
m% ol77am9chl4sp8cpx2
v% ol47am34chl12sp5cpx2
m ol59.2am6.8chl3.1sp6.4cpx1.5

D (0.8 wt% H_2O)
m% ol75am8sp11opx4cpx2
v% ol52am35sp7opx4cpx2
m ol62.3am6.8sp9.5opx3.1cpx1.5

E (0.4 wt% H_2O)
m% ol82am4an7opx5cpx2
v%ol62am20an11opx5cpx2
m ol74.8am3.8an6(opx2.6mgts2)cats1.5

F (0.4 wt% H_2O)
m% ol80am4an7opx5cpx2sp2
v% ol60am20an11opx5cpx2sp2
m ol72.8am3.8an6opx4.6cats1.5sp2

G (0.4 wt% H_2O)
m%ol79am4an7opx5sp4cpx2
v% ol59am20an11opx5sp3cpx2
m ol71.3am3.8an6opx4.6sp3.5cpx1.5

H (0 wt% H_2O)
m% ol69opx14cpx9an6sp2
v% ol58opx17cpx12an12sp2
m ol69opx14(cpx7.5cats1.5)an6sp2

J (2.1 wt% H_2O)
m% ol81am5chl4an7cpx2opx1
v% ol54am19chl13an11cpx2opx1
m ol67.8am3.8chl3.5an6cpx1.5opx1.1

K (2.4 wt% H_2O)
m% ol82am5chl5an6cpx2
v% ol53am20chl15an10cpx2
m ol65.6am4chl3.9an5.1cpx1.5

L (0 wt% H_2O)
m% ol71opx14cpx9an6
v% ol60opx17cpx12an12
m ol71(opx12mgts2)(cpx7.5cats1.5)an6

M (0 wt% H_2O)
STARTING COMPOSITION
m% ol59opx20cpx15sp6
v% ol51opx25cpx20sp4
m ol59opx20(opx18mgts2)cpx15(cpx13.5cats1.5)sp6

N (0 wt% H_2O)
m% ol69cpx16gar6opx9
v% ol57cpx20gar14opx10
m ol65(opx6mgts2)(cpx13.5cats1.5gar6

O (0 wt% H_2O)
m% ol70cpx16gar17opx6
v% ol57cpx20gar17opx6
m ol65(opx3mgts2)cpx15gar7.5

P (4.8 wt% H_2O)
m% ol71chl13am6cpx9
v% ol38chl35am20cpx8
m ol50.2chl9.5am4.2cpx6.6

Q (7.6 wt% H_2O)
m% chl16atg2ol57cpx26
v% chl32atg29ol23cpx16
m chl9atg1ol32cpx14.6

S (4.5 wt% H_2O)
m% ol57chl12cpx19opx13
v%ol35chl35cpx18opx12
m ol46chl9.5cpx15opx10.5

T (10.5 wt% H_2O)
m% atg6chl30cpx49phA15
v% atg45chl29cpx15phA11
m atg1.68chl9cpx14.6phA4.5

U (6.5 wt% H_2O)
m% opx51chl14phA14cpx22
v% opx33chl31phA22cpx15
m opx24.3chl9.5phA9.2cpx15

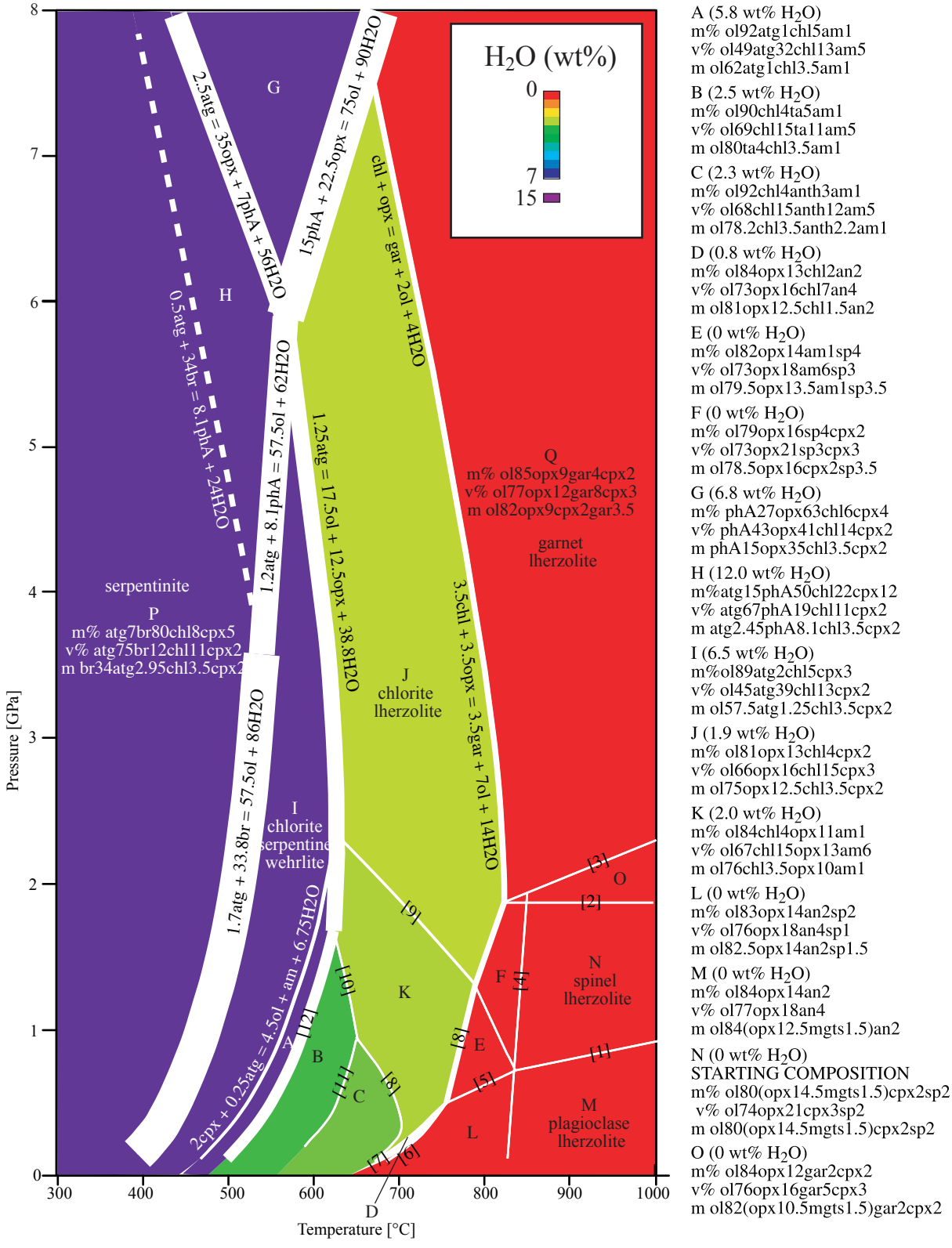

A (5.8 wt% H_2O)
m% ol92atg1chl5am1
v% ol49atg32chl13am5
m ol62atg1chl3.5am1

B (2.5 wt% H_2O)
m% ol90chl4ta5am1
v% ol69chl15ta11am5
m ol80ta4chl3.5am1

C (2.3 wt% H_2O)
m% ol92chl4anth3am1
v% ol68chl15anth12am5
m ol78.2chl3.5anth2.2am1

D (0.8 wt% H_2O)
m% ol84opx13chl2an2
v% ol73opx16chl7an4
m ol81opx12.5chl1.5an2

E (0 wt% H_2O)
m% ol82opx14am1sp4
v% ol73opx18am6sp3
m ol79.5opx13.5am1sp3.5

F (0 wt% H_2O)
m% ol79opx16sp4cpx2
v% ol73opx21sp3cpx3
m ol78.5opx16cpx2sp3.5

G (6.8 wt% H_2O)
m% phA27opx63chl6cpx4
v% phA43opx41chl14cpx2
m phA15opx35chl3.5cpx2

H (12.0 wt% H_2O)
m%atg15phA50chl22cpx12
v% atg67phA19chl11cpx2
m atg2.45phA8.1chl3.5cpx2

I (6.5 wt% H_2O)
m%ol89atg2chl5cpx3
v% ol45atg39chl13cpx2
m ol57.5atg1.25chl3.5cpx2

J (1.9 wt% H_2O)
m% ol81opx13chl4cpx2
v% ol66opx16chl15cpx3
m ol75opx12.5chl3.5cpx2

K (2.0 wt% H_2O)
m% ol84chl4opx11am1
v% ol67chl15opx13am6
m ol76chl3.5opx10am1

L (0 wt% H_2O)
m% ol83opx14an2sp2
v% ol76opx18an4sp1
m ol82.5opx14an2sp1.5

M (0 wt% H_2O)
m% ol84opx14an2
v% ol77opx18an4
m ol84(opx12.5mgts1.5)an2

N (0 wt% H_2O)
STARTING COMPOSITION
m% ol80(opx14.5mgts1.5)cpx2sp2
v% ol74opx21cpx3sp2
m ol80(opx14.5mgts1.5)cpx2sp2

O (0 wt% H_2O)
m% ol84opx12gar2cpx2
v% ol76opx16gar5cpx3
m ol82(opx10.5mgts1.5)gar2cpx2

Figure 3. Phase diagram for depleted lherzolite (see notes to Figure 2). Most of the bound H_2O is lost at □500□C. [1] 4fo + 2an = 2en + 2di + 2sp; [2] 4en + 2sp = 2py + 2fo; [3] 1.5py = 1.5en + 1.5mgts; [4] 1.5en + 1.5sp = 1.5fo + 1.5mgts; [5] tr + 2sp = 0.5en + 3fo + 2an + H_2O; [6] 1.5clin = 1.5en + 1.5fo + 1.5sp + 6H_2O; [7] 2clin + tr = 5fo + 2.5en + 2an + 9H_2O; [8] 3.5clin = 3.5en + 3.5fo + 3.5sp + 14H_2O; [8] 2.2fo + 2.2anth = 9.9en + 2.2H_2O; [9] 1fo + 1tr = 2.5en + 2di + 1H_2O; [10] 4a + 4fo = 10en + 4H_2O; [11] 4ta + 1.8fo = 2.2anth + 1.8H_2O; [12] atg = 4ta + 18fo + 27H_2O.

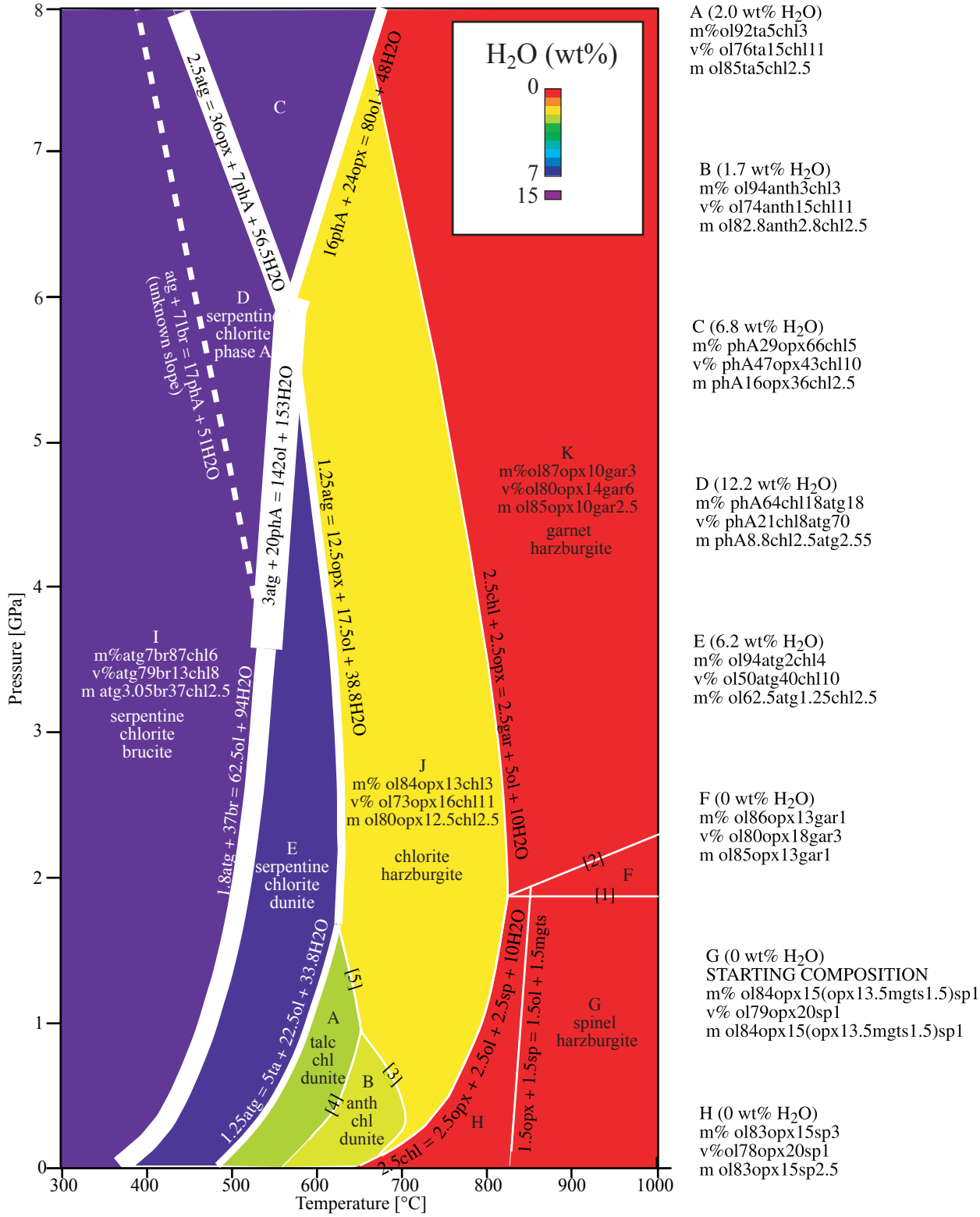

Figure 4. Phase diagram for harzburgite (see notes to Figure 2). Most of the bound H_2O is lost at □500□C. [1] 2en + sp = py + fo; [2] 1.5py = 1.5en + 1.5mgts; [3] 2.8fo + 2.8anth = 12.5en + 2.8H_2O; [4] 5ta + 2.2fo = 2.8anth + 2.2H_2O; [5] 5ta + 5fo = 12.5en + 5H_2O.

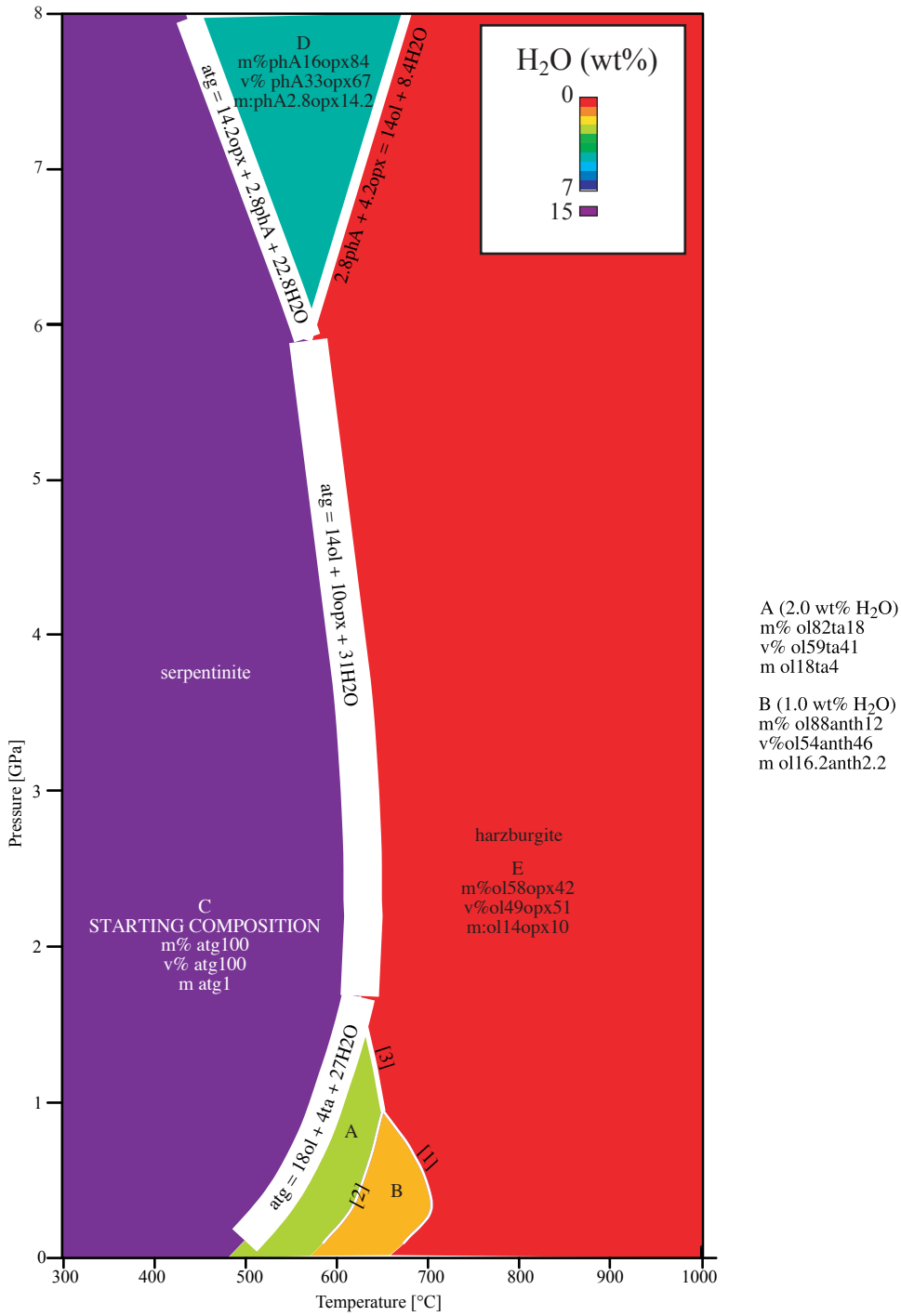

Figure 5. Phase diagram for serpentinite (see notes to Figure 2). [1] 2.2fo + 2.2anth = 9.9en + 2.2H_2O; [2] 1.8fo + 4ta = 2.2anth + 1.8H_2O; [3] 4fo + 4ta = 10en + 4H_2O.

[8] The strength of our approach is that the mineral parageneses, compositions, and modes that we used to construct Figure 1 actually occur in naturally metamorphosed high-pressure rocks. Some disadvantages include (1) Assuming that the entire crust is of MORB composition is incorrect for the lower oceanic crust, which tends to be more aluminous and more magnesian [Dick et al., 2000]. (2) This assumption is also incorrect for portions of the crust that are altered, which are most notably enriched in Al and Ca relative to MORB (Table 2) [Staudigel et al., 1996] and which would likely stabilize additional hydrous Ca-Al silicates [Pawley and Holloway, 1993; Poli and Schmidt, 1997]. (3) In this paper, we consider only anhydrous and fully hydrated MORB, whereas the oceanic crust is heterogeneously hydrated. The end-member cases that we treat here can be considered to bound all possible hydration states.

Table 5. Mineral Modes for "Starting Compositions" of Ultramafic Rocks[a]

	Enriched Lherzolite	Harzburgite	Harzburgite	Serpentinite
di, diopside	18	3		
en, enstatite	22	19	18	
fs, ferrosilite	2	2	2	
hed, hedenbergite	2			
atg, antigorite				100
fo, forsterite	46	67	71	
fa, fayalite	5	7	8	
spinel + rutile + sphene	2	1		
mt, magnetite	2	1		

[a]In units of volume percent. Mineral abbreviations from *Holland and Powell* [1998].

Table 7. Compositions Used to Convert Abundances of Minerals With Solid Solutions to Abundances of End-Member Minerals[a]

Mineral	Composition
Olivine	$forsterite_{90}fayalite_{10}$
Clinopyroxene	$diopside_{90}hedenbergite_{10}$
Orthopyroxene	$enstatite_{90}ferrosilite_{10}$
Garnet	$pyrope_{66}almandine_{24}grossular_{10}$
Spinel	$magnetite_{50}spinel_{50}$
Chlorite	$clinochlore_{90}daphnite_{10}$
Plagioclase	$anorthite_{86}albite_{14}$
Amphibole	$tremolite_{35}pargasite_{60}ferro\text{-}actinolite_{05}$

[a]In units of mole percent.

3.2. Ultramafic Rocks

[9] Lherzolite and harzburgite are the common enriched and depleted rock types of the upper mantle; depleted lherzolite is intermediate. Harzburgite (olivine + orthopyroxene) is the dominant rock type in mantle wedges and the uppermost oceanic mantle; the lherzolite (olivine + orthopyroxene + clinopyroxene) models are included for completeness. Because of considerable interest in serpentinization, we model the bulk composition of pure serpentinite, but note that all the other ultramafic bulk compositions we model also are largely serpentine at lower temperature.

[10] Phase diagrams for lherzolite, depleted lherzolite, harzburgite, and serpentinite (Figures 2–5) were constructed with a different technique than that used for mafic rocks. We used four sets of mineral compositions and modes as "starting compositions" (labeled in Figures 2–5; see Table 5); the lherzolite is from *Ernst* [1977], the depleted lherzolite and harzburgite are from *Lippard et al.* [1986], and we chose the bulk composition of the serpentinite as Mg_{95} antigorite. These are typical upper mantle bulk compositions. The volume and molar proportions of each mineral that make up each rock are shown in Figures 2–5. A reaction network was then created around each of these "starting compositions." Using mineral compositions reported from meta-ultramafic rocks worldwide, we calculated two separate sets of activities for high pressure and low pressure, using either ideal mixing or the program "A-X" by T. Holland and R. Powell (Table 6). The P–T positions of the reactions among the phases were then calculated as Mg-end-member reactions in the Ca-Fe^{2+}-Mg-Al-Si-H-O system, using Thermocalc [*Powell et al.*, 1998]. Thermocalc calculations of phase relations at $P > 5$ GPa were then modified in light of recent experiments by *Luth* [1995], *Ulmer and Trommsdorff* [1995], *Wunder and Schreyer* [1997], *Bose and Navrotsky* [1998], *Wunder* [1998], and *Pawley* [2000]. The calculated mineral abundances were then converted to end-member mineral abundances using the formula in Table 7. Although these phase diagrams are considered to be very reliable, there is still considerable ambiguity regarding the relations among phases in ultramafic rocks at high pressure and low temperature; e.g., the slope of the reaction antigorite + brucite = phase A + H_2O is poorly constrained.

3.3. Other Compositions

[11] As a basis for comparing the properties of the metamorphosed rocks to unaltered rocks, we used mineral composition and mode data from holocrystalline MORBs [*Ayuso et al.*, 1976; *Mazzullo and Bence*, 1976; *Cann*, 1981; *Perfit and Fornari*, 1983], diabase [*Alt et al.*, 1993], olivine gabbro [*Tiezzi and Scott*, 1980; *Browning*, 1984; *Lippard et*

Table 6. Activities Used to Construct Ultramafic Phase Diagrams[a]

Phase	Activity Model	High-Pressure Activity	Reference	Low-Pressure Activity	Reference
fo, forsterite	ideal	0.91	MR98	0.80	L86, MR98
di, diopside	HP98	0.75	Z95	0.96	L86, P87
mgts, Mg-tschermak	HP98	0.04	Z95	?	L86, P87
en, enstatite	HP98	0.81	C83	0.79	L86, P87
cats, Ca-tschermak	HP98	0.1	Z95	?	L86, P87
py, pyrope	HP98	0.3	C83, Z95	0	
sp, spinel	ideal	0.8	C83, MR98	0.6	MR98
clin, clinochlore	HP98	0.7	LZ98, Z95	0.4	P87
atg, antigorite	ideal	0.95		0.95	P87
br, brucite	ideal	1		1	
ta, talc	ideal	0.78	LZ98	0.97	P87
an, anorthite	HP98	0		0.86	MR98
anth, anthophyllite	ideal	0		0.5	P87
tr, tremolite	HP98	0.3	C83, LZ98, Z95	0.6	P87
phA, phase A	ideal	0.95		0	
H_2O	HP98	0–1		0–1	

[a]Mineral abbreviations from *Holland and Powell* [1998]. C83, *Carswell et al.* [1983]; HP98, *Holland and Powell* [1998]; L86, *Lippard et al.* [1986]; LZ98, *Liou and Zhang* [1998]; MR98, *McDonough and Rudnick* [1998]; P87, *Peacock* [1987]; Z95, *Zhang et al.* [1995].

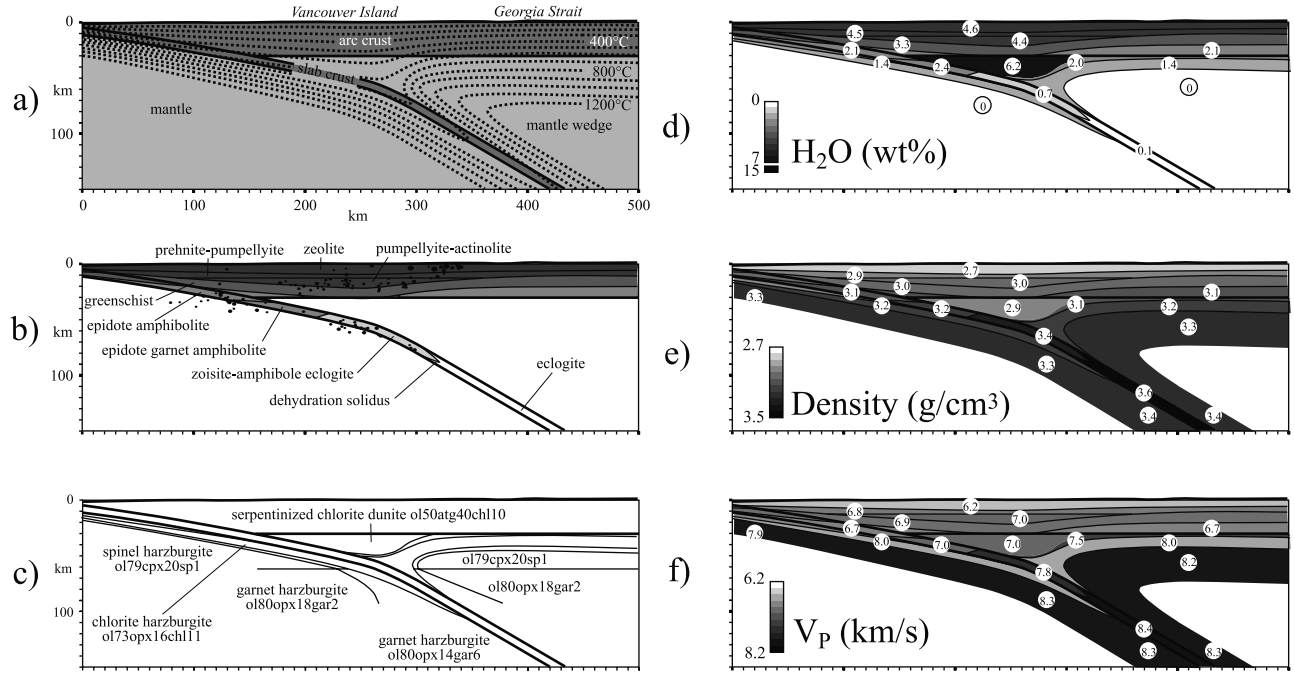

Figure 6. Calculated properties of the Cascadia subduction zone along a transect through southern Vancouver Island. (a) Geology and isotherms [*Hacker et al.*, 2003]. (b) Calculated phase relations in mafic crust and observed seismicity [*Rogers*, 1998]. Anhydrous eclogite formation is predicted to occur at 80–90 km depth in the slab. (c) Calculated phase relations in ultramafic rock. Numbers indicate vol % of minerals: anth, anthophyllite (amphibole); atg, antigorite (serpentine); br, brucite; clin, clinochlore (chlorite); en, enstatite (orthopyroxene); fo, forsterite (olivine); sp, spinel; py, pyrope (garnet). (d) Calculated maximum H_2O contents. Downgoing, hot slab mantle is nearly anhydrous, and only the tip of the mantle wedge can contain substantial H_2O. (e) Calculated densities. Density of mantle wedge is low because of maximum possible hydration is assumed. (f) Calculated *P* wave speeds. Wave speed of mantle wedge is low because maximum possible hydration is assumed.

al., 1986; *Elthon*, 1987; *Robinson et al.*, 1989], wehrlite, and olivine clinopyroxenite [*Lippard et al.*, 1986]. We do not model the physical properties of typical glassy ocean floor basalt because porosity and cracks play a dominant role in such rocks.

4. Computing Subduction Zone Pressures and Temperatures

[12] Temperatures in subduction zones have been calculated using numerical [e.g., *Toksöz et al.*, 1971; *Peacock*, 1990] and analytical [e.g., *Royden*, 1993; *Davies*, 1999] solutions. As an illustration, we show the thermal model of *Hacker et al.* [2003] for southern Vancouver Island (Figure 6a). Pressures were calculated using fixed densities of 1.0, 2.7, 3.0, and 3.3 g/cm^3 for water, continental crust, oceanic crust, and mantle, respectively.

5. Superimposing Phase Relations

[13] Onto a subduction zone cross section depicting P, T, and rock compositions, we overlayed the different metamorphic mineral assemblages computed in step 2. Figures 6b and 6c show the results for mafic rock and harzburgite, respectively. The diagrams are constructed assuming that the activity of $H_2O = 1$ (or that $P_{H2O} = P_{lithostatic}$; i.e., rocks are H_2O saturated) and that equilibrium obtains; these assumptions cannot be correct everywhere and are addressed partially in a later section. If the activity of $H_2O < 1$, phase boundaries (Figures 2–5) that involve the gain or loss of H_2O shift to favor anhydrous minerals.

6. Superimposing Rock Physical Properties

[14] From the mineral physical properties calculated at elevated P and T in step 1, we derive density and H_2O contents using a linear (Voigt) average and derive V_P and V_S from bulk and shear moduli determined for aggregates using a Voigt-Reuss-Hill average [*Hill*, 1952], all weighted by mineral proportions determined in step 2. Hashin-Shtrickman bounds on the same rocks reproduce the Voigt-Reuss-Hill averages to ±0.4%, so the simpler averaging method should suffice. The results are shown in Figures 7–13. As a test, we compare our calculated values with laboratory measurements of rocks in Figure 14. We used the measurements of 26 mostly mafic rocks by *Kern et al.* [1999] because that study also reported the proportions of minerals in the tested samples. At 60 MPa, 20°C (Figure 14b) and 60 MPa, 600°C (Figure 14c), our calculated V_P values exceed those of Kern et al. by ~2 and ~3%, respectively, likely because 60 MPa may not be sufficient to close microcracks in experimental samples. *Christensen* [1974] reported V_P

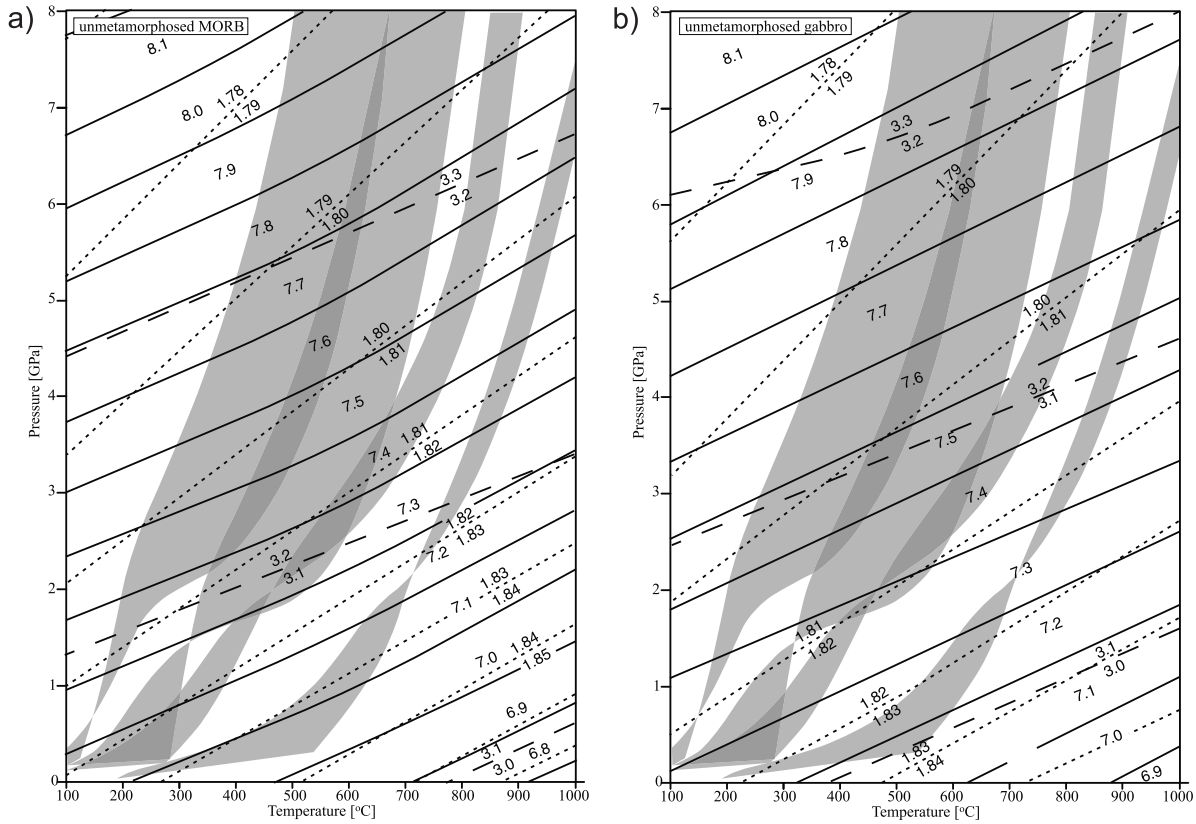

Figure 7. *P* wave speeds (6.x–8.x km/s), densities (3.x g/cm^3), and V_P/V_S (1.xx) of (a) unmetamorphosed MORB and (b) unmetamorphosed gabbro. Differences are due solely to differences in mineralogy. Shading shows PT paths for Tohoku, Nankai, Costa Rica, and Cascadia subducted crust from *Peacock and Wang* [1999] and *Hacker et al.* [2003].

and mineral modes, but not mineral compositions, for two eclogites, a dunite, and a pyroxenite. Our calculations reproduce his measured 3.0 GPa V_P values to better than 1%. We also compared our calculations to rock V_P values reported by *Christensen and Mooney* [1995], even though their mineral modes and compositions are unknown to us (Figures 14d–14f). In spite of this, we reproduce their V_P values at elevated P and T to within 2%. Of particular relevance to subduction zones, we calculate $\Delta V_P = -15\%$ and $\Delta V_S = -19\%$ for gabbro relative to dunite, in excellent agreement with *Christensen*'s [1996] measured values of $\Delta V_P = -14\%$ and $\Delta V_S = -18\%$. We consider all of this to be excellent agreement, considering that the mineral compositions (and in some cases, proportions) of the tested samples are unknown, and that the difference in V_P across the compositional ranges of, for example, olivine and plagioclase are 25% and 16%, respectively.

[15] The values we calculate for MORB composition are significantly different than those for a pure Ca-Mg-Al-Si-H-O system such as that used by *Helffrich* [1996]. One mole of an Fe-bearing mineral requires more wt % Fe than one mole of a Mg-bearing mineral. Thus rocks composed of Fe-bearing minerals contain less weight percent H_2O. Also, replacement of Mg by Fe affects density much more than elastic moduli, so seismic velocities correlate negatively with density for such substitutions. Our Fe-bearing rocks are also, as a result, roughly 4% denser and have seismic velocities that are ~4% slower.

[16] Our more detailed treatment of metamorphism results in significantly different predictions than previous studies. For example, *Furlong and Fountain* [1986] calculated the *P* wave velocities of mafic rocks using a three-part model of gabbro (V_P = 7.0–7.2 km/s), garnet granulite (V_P = 7.2–7.8 km/s), and eclogite (V_P = 7.8–8.2 km/s) (see their Figures 6 and 7). Our Figure 8 shows that metamorphism yields a much broader range of more distinctive velocities, and much slower velocities (6.5 km/s for mafic granulite, for instance). A simple two-part model of gabbro and eclogite (Figure 8c) captures the essence of the *Furlong and Fountain* [1986] calculation, extends it to 8 GPa, and emphasizes the resultant simplification of a two- or three-part model for mafic rocks.

7. Uncertainties

[17] There are many sources of uncertainty inherent in calculating rock properties from laboratory physical property measurements. These uncertainties can be grouped into three categories: (1) uncertainty in single-mineral thermoelastic parameters, (2) uncertainty due to calculational approximations, and (3) uncertainty arising from converting single-crystal data to rock properties.

7.1. Single-Mineral Thermoelastic Parameters

[18] The thermoelastic parameters that most significantly influence single-crystal property calculations are the den-

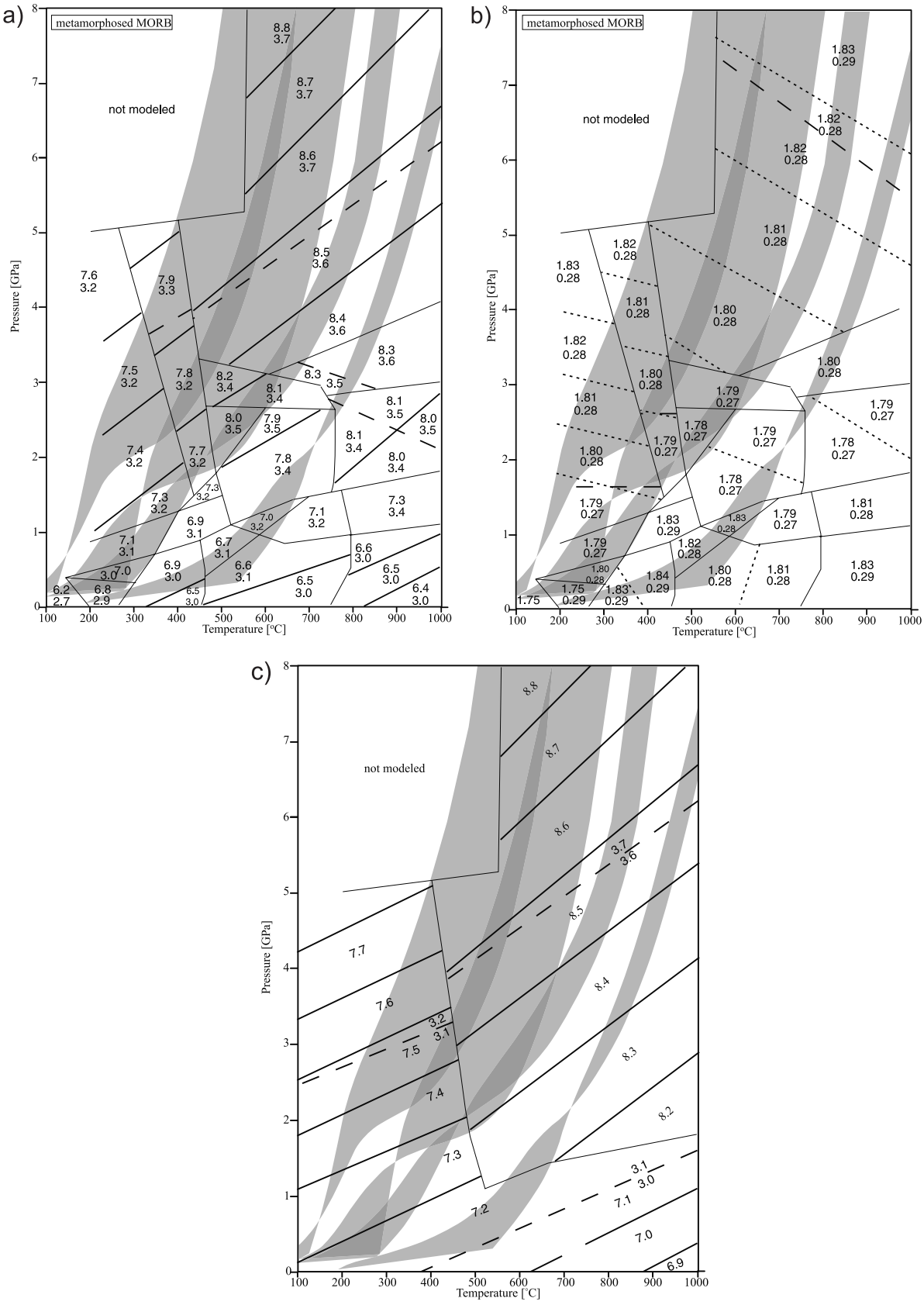

Figure 8. (a) *P* wave speeds (6.x–8.x km/s) and densities (3.x g/cm^3) of metamorphosed MORB. (b) V_P/V_S (1.xx) and Poisson's ratio (0.xx) of metamorphosed MORB. (c) *P* wave speeds for a simple, two-part (gabbro and eclogite) mafic rock model; such a simple model obscures most of the important changes seen in the complete model.

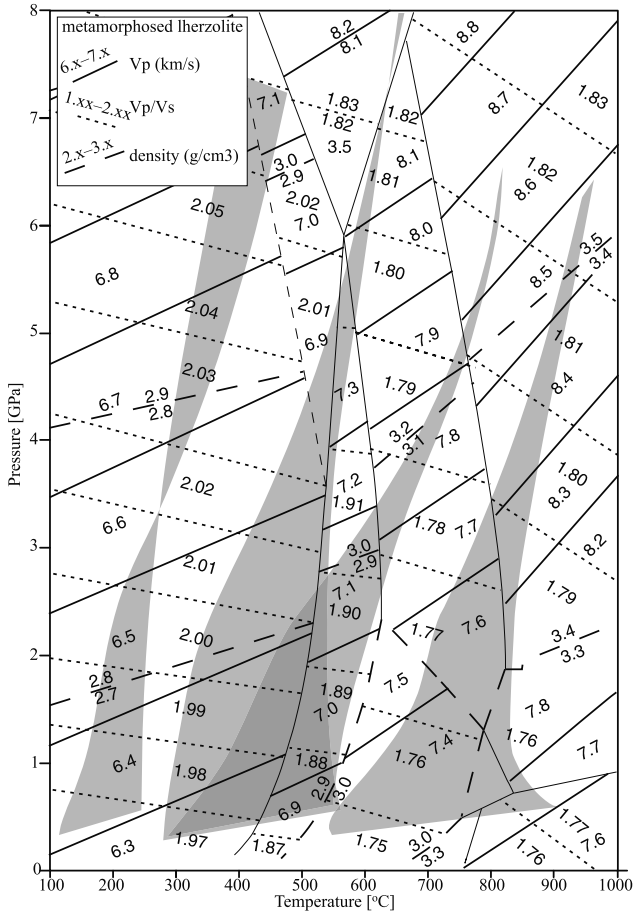

Figure 9. *P* wave speeds (6.x–8.x km/s), densities (3.x g/cm^3), and V_P/V_S (1.xx) of metamorphosed lherzolite; shading shows PT paths of upper 8 km of subducted mantle in Tohoku, Nankai, Costa Rica, and Cascadia subduction zones. The presence of antigorite (serpentine) causes a marked change in physical properties.

sities, thermal expansivities and elastic moduli. Densities are generally known to better than 0.15% [*Smyth and McCormick*, 1995], although minerals with variable structural state (e.g., mica polytypes) have different densities (<3%), an issue that we do not consider. Various investigators have reported thermal expansivities for simple minerals such as olivine that vary by 14% [*Fei*, 1995], although the precision of individual measurements is better than 2% [*Anderson and Isaak*, 1995]; for many minerals, including most pyroxenes, $\partial\alpha/\partial T$ has not been measured. Bulk and shear moduli measured in different laboratories for simple minerals such as pyrope and diopside differ by 2% and 3%, respectively [*Bass*, 1995; *Knittle*, 1995], although the precision of individual measurements is better than 1% [*Anderson and Isaak*, 1995]. Uncertainties for individual modulus and thermal expansitivity measurements translate to uncertainties of ~1.5% for individual γ_{th} and Γ measurements and determinations from different laboratories should vary no more than ~10%. Moreover, the general dearth of $\partial\mu/\partial T$ and $\partial K_T/\partial P$ determinations mean that Γ for most minerals must be approximated as $\Gamma = \delta_T$ [*Anderson and Isaak*, 1995], and δ_T must be approximated as $\delta_T \approx \gamma_{th} + K'_T$ [*Anderson et al.*, 1992]. The Grüneisen parameter γ_{th}, can be measured to ~2% [*Anderson and Isaak*, 1995] but is unmeasured for most minerals. As a single example of the kind of uncertainty inherent in values for specific minerals, consider zoisite. *Pawley et al.* [1998] reported $K_T = 127 \pm 4$ GPa assuming $\partial K_T/\partial P = 4$, *Grevel et al.* [2000] reported $K_T = 125.1 \pm 2.1$ GPa assuming $\partial K_T/\partial P = 4$ and $K_T = 137$ GPa if $\partial K_T/\partial P = 0.5$, and *Comodi and Zanazzi* [1997] reported $K_0 = 102.0 \pm 6.5$ GPa and $\partial K_T/\partial P = 4.8$. At 6 GPa, these different values translate into K_T values of 151, 149, 140, and 131 GPa, or bulk sound velocity variations of +3%. *Grevel et al.* [2000] argued that none of these studies can distinguish $\partial K_T/\partial P$ from 4.

[19] Monte Carlo simulations indicate that for a simple mineral with a reasonably well-determined set of thermoelastic parameters (e.g., garnet), the uncertainties on single measurements imply <0.5% uncertainty in V_P and V_S and <1% uncertainty in elastic moduli calculated at elevated pressure and temperature (e.g., 800°C, 4 GPa). If we consider the much larger variation exhibited by measurements from different laboratories, the calculated uncertainties increase to <2% uncertainty in V_P and V_S and <4% uncertainty in elastic moduli. Fortunately, the polymineralic nature of rocks minimizes sensitivity to error in any single measurement.

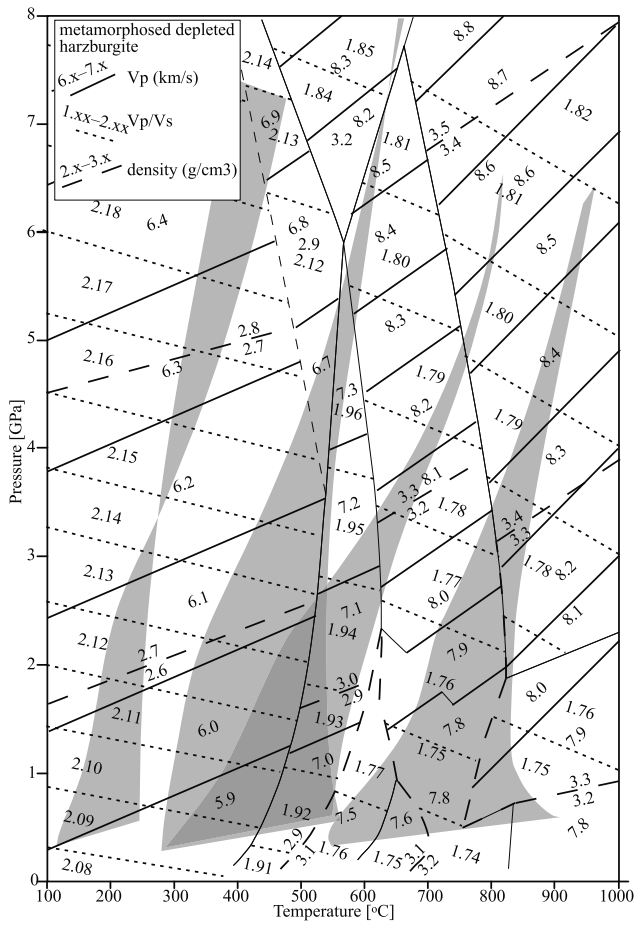

Figure 10. Properties of metamorphosed depleted lherzolite (see Figure 9 caption). The presence of antigorite (serpentine) causes a marked change in physical properties.

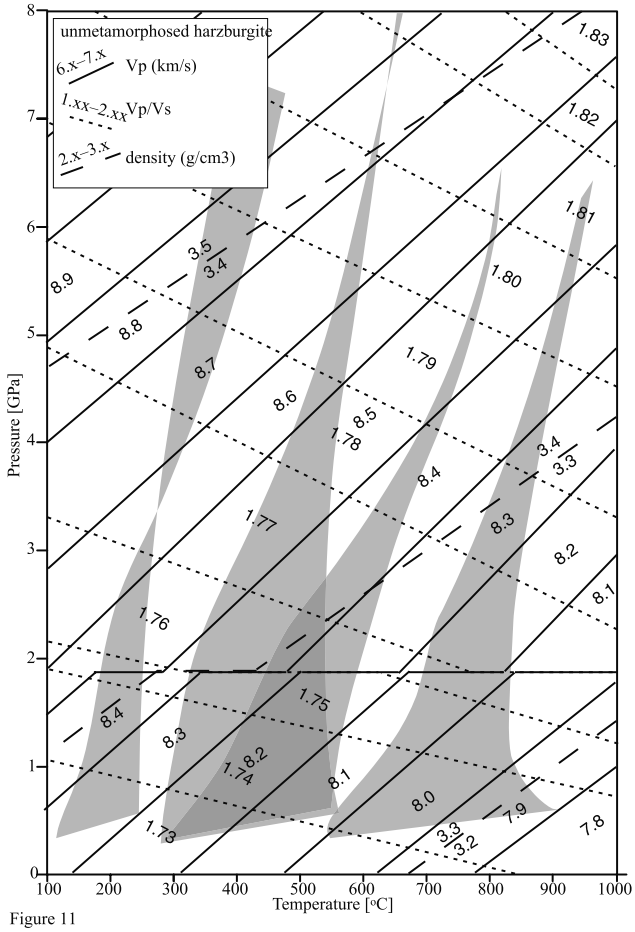

Figure 11

Figure 11. Properties of unmetamorphosed spinel harzburgite (see Figure 9 caption). Physical properties change monotonically.

7.2. Calculational Approximation

[20] Our calculation procedure makes three important assumptions (see Appendix A). We use *Holland and Powell*'s [1998] approximation for thermal expansivity, which appears to give excellent fits to the data [*Pawley et al.*, 1996]. We use a third-order finite strain approximation. We ignore the second pressure derivatives of the elastic moduli. Although small uncertainties may arise from these approximations, the general lack of higher-order information on derivatives makes any more exact procedure difficult to verify.

8. Comparing Predictions to Observations

[21] As a simple example of the use of these calculations, we compare observed and predicted wave speeds for (1) unsubducted oceanic lithosphere, (2) subducting slabs, and (3) the mantle of the overriding plate in a subduction zone.

8.1. Oceanic Lithosphere Velocities and Mineralogy

[22] *White et al.* [1992] and *Mutter and Mutter* [1993] summarized the seismic velocity structure of oceanic crust and uppermost mantle obtained from seismic refraction measurements worldwide. Figure 15 compares the inferred lower crust and upper mantle velocities measured in the studies cited by *White et al.* [1992] with our calculated velocities. Each velocity measurement and calculation is compared at the appropriate in situ temperature and pressure for lower crust and mantle of the ages reported by White et al. The compilation of *White et al.* [1992] does not, in general, differentiate azimuths, and the upper mantle is known to have substantial anisotropy (e.g., *Pn* can vary by up to 5% with azimuth [*Shearer and Orcutt*, 1986]), so some of the observed variation may be due to anisotropy. Our calculated wave speeds represent isotropic averages, so actual measurements from anisotropic peridotites should lie within ~2.5% (0.2 km/s) of these calculations, and variations smaller than that should not be considered to necessarily reflect differences in composition.

[23] The observed lower crustal velocities range from 6.5 to 7.8 km/s, with most values in the range of 6.6–7.6 km/s. The velocities we calculate for anhydrous rocks typical of layer 3 (gabbronorite and olivine gabbro) are toward the middle of this range. The speeds slower than 7.0 km/s observed from the lower crust imply alteration or geological heterogeneity of the type described by *Karson* [1998] and *Dilek et al.* [1998]. If homogeneous alteration of a single rock type is responsible, these velocities are best matched by amphibolite-facies alteration (1.3 wt % H_2O); however, in even the most altered sections of the lower crust alteration does not reach 100% [cf. *Dick et al.*, 1991]. If these slow velocities are the result of complex mixtures of mafic rock and serpentinized ultramafic rock [e.g., *Karson*, 1998], mixtures of gabbro plus 15–30 vol % antigorite can account for the observed velocity shifts of −0.4 to −0.6 km/s because antigorite has velocities of 5.7–5.8 km/s at these conditions. Because serpentine has an unusual Poisson's ratio [*Christensen*, 1996], better oceanic V_S measurements would help resolve these two possibilities. Observed velocities greater than our predicted gabbro speeds are well matched by a mixture of gabbro and wehrlite or olivine clinopyroxenite. Such waves are likely sampling the mafic/ultramafic transition zone, which is petrologically part of the crust, but seismically part of the mantle. Note that there is no persuasive indication that lower crustal wave speeds change with age of the lithosphere in any way other than expected from simple cooling (i.e., the measurements of White et al. track our calculated curves for various rock types), implying that the structure and composition of the lithosphere are determined at or near the ridge axis and not significantly modified thereafter.

[24] Spinel harzburgite is a good explanation for most of the faster observed upper mantle velocities. The slower velocities could be wehrlite or olivine clinopyroxenite, as suggested above for the lowermost crust, but the summary of *White et al.* [1992] shows that the thickness of the zones with measured velocities that are faster than gabbro and slower spinel harzburgite velocities is much greater than the typical 500-m thickness of ophiolite transition zones [*Coleman*, 1977]. Thus these slowest parts of the uppermost mantle are likely harzburgite with up to 20% alteration to serpentine, brucite, and chlorite (~2.4 wt% H_2O).

[25] Our approach has some advantages over other techniques. For example, *Carlson* [2001] demonstrated that velocities inferred for end-member rock types from meas-

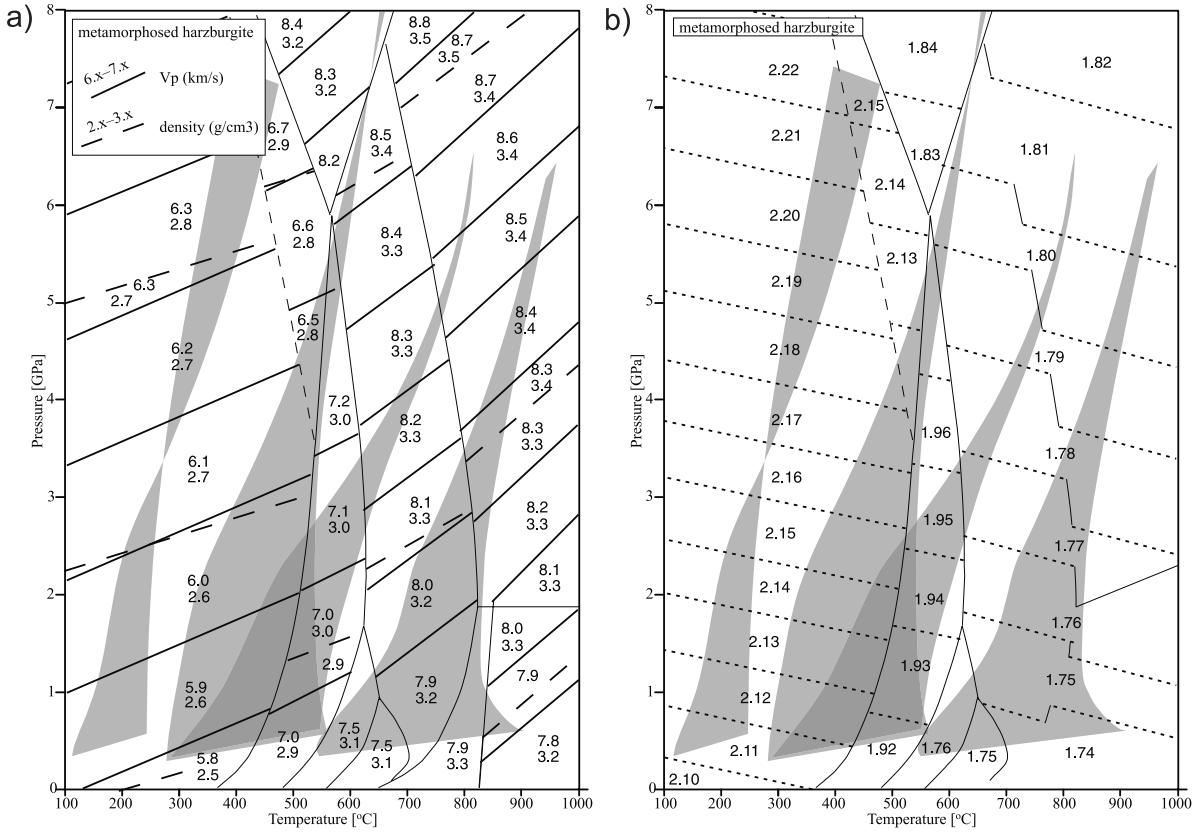

Figure 12. Properties of metamorphosed harzburgite (see Figure 9 caption). The presence of antigorite (serpentine) causes a marked change in physical properties.

urements of Ocean Drilling Program (ODP) cores 504B and 735B do not compare well with velocities calculated from single-crystal measurements averaged by the Voigt-Reuss-Hill (VRH) technique or with seismic profiles of the oceanic lithosphere. In contrast, as illustrated in Figure 14, our calculated velocities compare well with rock velocities measured in the laboratory and with those inferred from seismological studies (Figure 15). We suspect that variable degrees of alteration and accessory minerals may be affecting properties of the field samples treated as end-member compositions. Our method permits the calculation of properties of unaltered rocks, whereas many laboratory velocity measurements are on rocks with incompletely described alteration.

8.2. Subducting Slab Velocities and Mineralogy

[26] Figure 16 extends the comparison among calculated wave speeds of rocks to a broader range of bulk compositions and pressures relevant to subducting slabs. Figure 16a shows that anhydrous gabbro is 9–12% slower than anhydrous harzburgite over subduction zone pressures and temperatures. This number is a good match to Figure 15, which shows that the observed velocity difference between typical uppermost mantle and uppermost layer 3 is ~15%. Figure 16 is a better way to compare crustal and mantle velocities than simply comparing gabbro to dunite [e.g., *Christensen*, 1996].

[27] Figure 16b shows *P* wave velocities of the various metamorphic facies for fully hydrated MORB versus anhydrous harzburgite. Metamorphosed, fully hydrated MORB is >15% slower than dry harzburgite at pressures <1.0 GPa, ~10% slower than harzburgite at temperatures <500°C, and ~3% slower when at zoisite- or amphibole-bearing eclogite facies. The fact that the *P* wave speed of anhydrous eclogite is indistinguishable from unaltered harzburgite has important implications for *P* wave tomography: velocity variations can only reflect differences in temperature. Figure 16c shows *P* wave velocities of the various metamorphic facies for fully hydrated MORB versus the various metamorphic facies for fully hydrated harzburgite. Velocities of metamorphosed MORB are ~5–15% slower than metamorphosed harzburgite at $T > 450$°C and $P < 1.5$ GPa, 15–30% faster at $T < 500$°C, ~3–4% faster at $T = 600$–800°C and $P > 1.5$ GPa, and similar at higher temperatures. Figures 16b and 16c thus encompass the entire range of wave speed differences expected between MORB and harzburgite with 0–100% alteration. In principal, one can solve for extent of hydration using the *P* wave speed.

[28] These diagrams serve as a useful starting point for interpreting the velocities of subducted slabs. In cold subduction zones such as Tohoku, abundant alteration of the mantle is thermodynamically permitted, leading to the potential for slow mantle wave speeds immediately above and below the slab crust (Figure 16c). If the crust and mantle are completely hydrated, the crust can be up to 22–40% faster than the mantle to great depth (Figure 16c). Most relatively cold subduction zones exhibit seismically slow

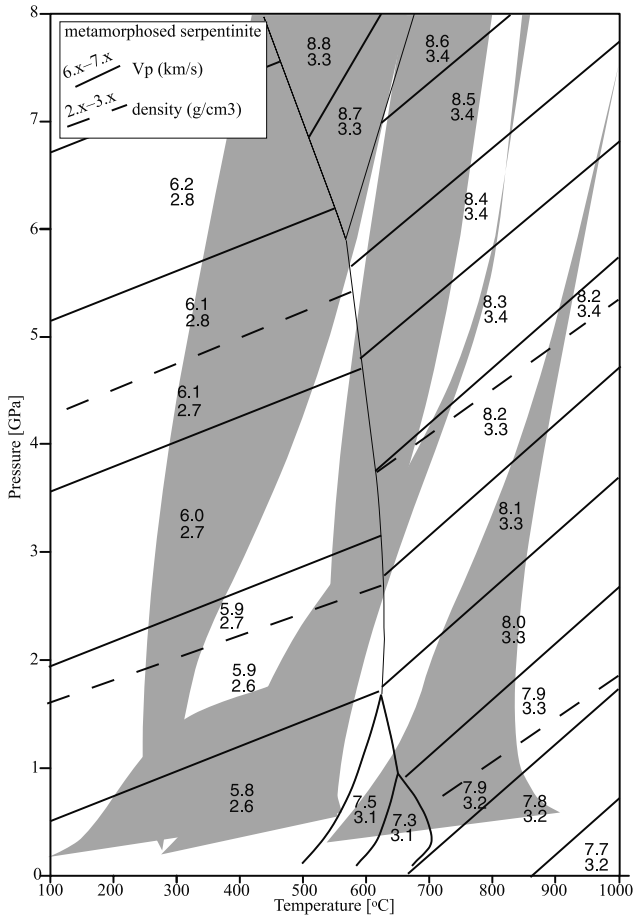

Figure 13. Properties of metamorphosed serpentinite (see Figure 9 caption).

rather than fast layers: the Mariana, Tohoku, Kurile, Aleutians, and Alaska slabs have 5–8% slow layers that persist to depths of 100–250 km [*Abers*, 2000]. This is incompatible with extensive alteration of the mantle (Figure 16c) but can be explained as a slab of metamorphosed MORB contained within partially altered harzburgite (i.e., intermediate between Figures 16b and 16c).

[29] Several seismic signals passing through the Tohoku slab (northern Honshu) have revealed a slow channel, of thickness comparable to subducted crust at the top of the slab [*Matsuzawa et al.*, 1986; *Iidaka and Mizoue*, 1991; *Abers*, 2000], potentially explainable in manner just described. The study of Matsuzawa et al. models *P-S* conversions by a layer 6% slower than the overlying mantle and 12% faster than that underlying it, between 60 and 150 km depth, whereas that of *Abers* [2000] explains dispersed body waves with a layer 6% slow and 4 km thick, largely between 100 and 150 km depth (Table 8). At these depths, subducted crust beneath Tohoku should be lawsonite-amphibole eclogite with V_P = 7.9 km/s if fully hydrated (Figure 8a and Table 8). The presence of a low velocity crust precludes extensive hydration of the mantle above and below, as at these P–T conditions hydrated ultramafic rocks should be 25–29% slower than hydrated gabbro (Figure 16c). By comparison, a hydrated metamorphosed gabbro should be 8% slower than unmetamorphosed mantle (Figure 16b). The slightly lower contrast observed here may reflect incomplete hydration; the difference in mantle wave speed above and below the crust may reflect less mantle hydration in the downgoing plate than within the mantle wedge. Alternatively, a combination of hydrated MORB overlying anhydrous, unmetamorphosed gabbro may explain these observations [*Hacker*, 1996].

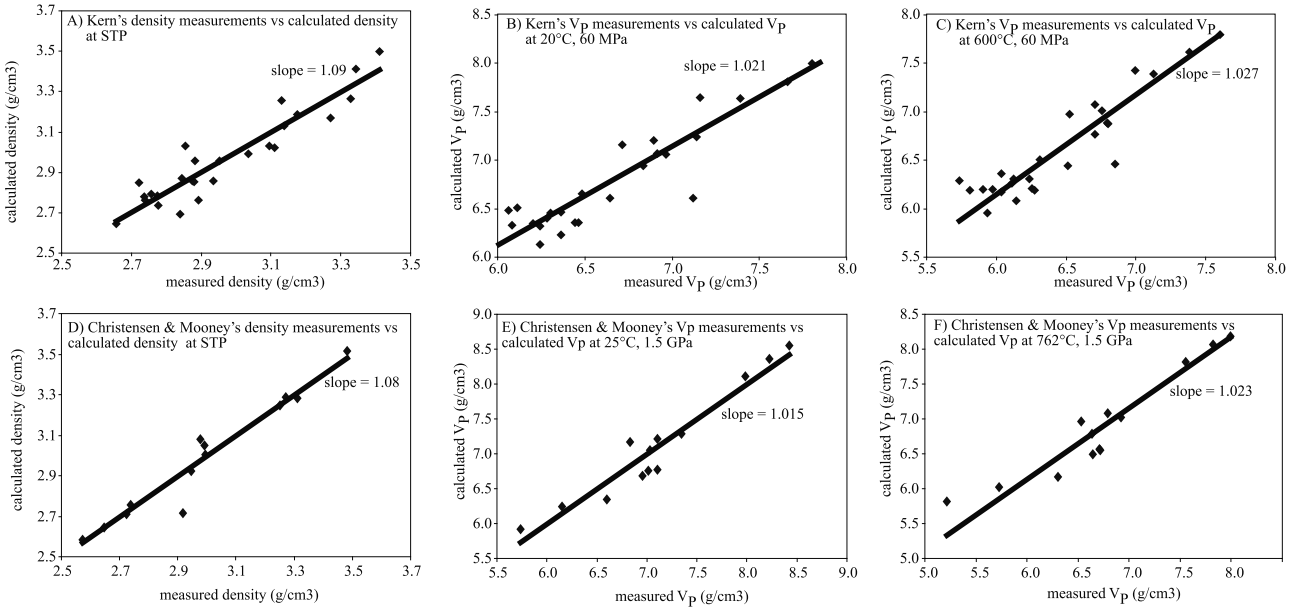

Figure 14. Rock properties measured in laboratories differ from our calculated properties for the same rocks by 1–2%. We assumed that (1) Mg/(Mg + Fe) = 0.75 for orthopyroxene, clinopyroxene, and biotite; (2) garnet has the composition $alm_{50}grs_{30}prp_{20}$, (3) all amphibole is hornblende; (4) Mg/(Mg + Fe) = 0.5 for chlorite; and plagioclase is $An_{50}Ab_{50}$.

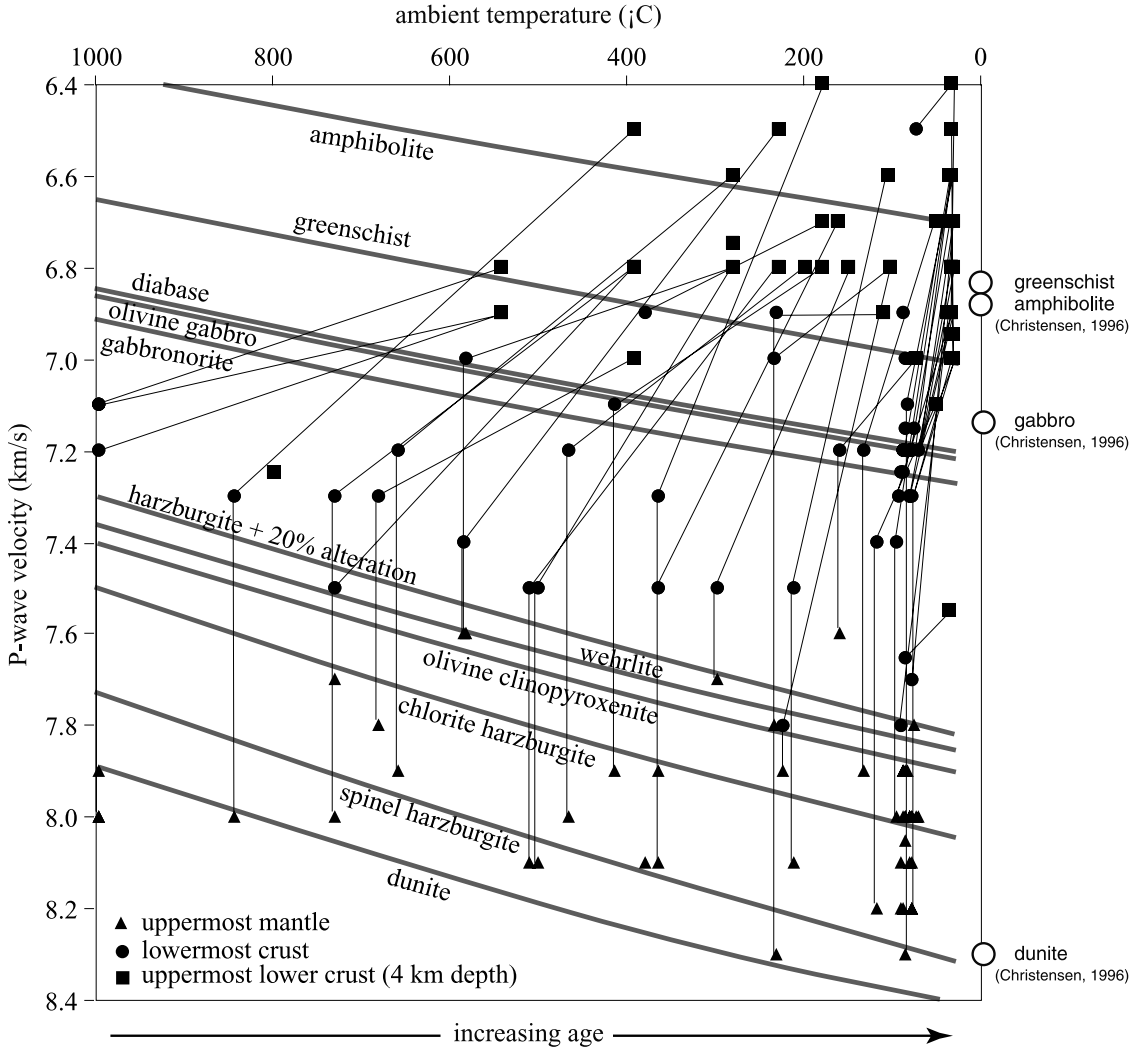

Figure 15. The observed *P* wave speeds for oceanic lower crust and mantle (triangles, circles, and dots from *White et al.* [1992]) compared with our calculated *P* wave speeds for various rocks at 200 MPa and indicated temperatures (gray curves). Subvertical lines connect measured uppermost lower crust, lowermost crust and uppermost mantle velocities at single locations; the temperatures shown for each datum were calculated from the lithosphere age reported by White et al., following *Sclater et al.* [1980]. Room temperature, 200 MPa measurements of *Christensen* [1996] shown along right side are slightly slower than our calculated velocities. Most uppermost mantle velocity measurements are best explained as spinel harzburgite. Most lower crust measurements are intermediate between gabbro and amphibolite, indicating partial hydration. Most lowermost crust measurements are consonant with a mixture of gabbro, wehrlite, and olivine clinopyroxenite, or harzburgite containing <20% hydrous minerals.

[30] The Tonga slab appears very different, as high-frequency precursors recorded in New Zealand may require a thin, high-velocity layer embedded in a relatively slow surrounding mantle [*Gubbins and Sneider*, 1991; *van der Hilst and Snieder*, 1996]. This inferred velocity profile, if correct, may be explainable as a consequence of extensive hydration of the mantle surrounding the subducted crust. Alternatively, the Tonga observations may be a path effect [*Abers*, 2000].

[31] In hot subduction zones such as Nankai, little hydration of the mantle is thermodynamically permitted (Figures 2–4), leading to fast predicted mantle wave speeds (Figures 16a and 16b). Fully hydrated mafic crust will be 16% slower than the mantle down to depths of ~35 km, ~4% slower down to ~70 km, and indistinguishable from the mantle at greater depth (Figure 16b). In contrast, anhydrous mafic crust will remain ~12% slower than the mantle until transformed to eclogite (Figure 16a). *Hori* [1990] examined seismic waves coming from the Philippine Sea plate subducting at the eastern end of the Nankai Trough, and noted that waves emanating from depths shallower than 40–60 km show two strong P and S phases each, the second traveling considerably slower than predicted from travel time tables. They interpreted the first *P* and *S* arrivals as traveling through the upper mantle of the downgoing plate at velocities of 8.2 and 4.7 km/s, respectively, and modeled the second phases as traveling through the subducted crust at V_P = 7.0 and V_S = 4.0 km/s

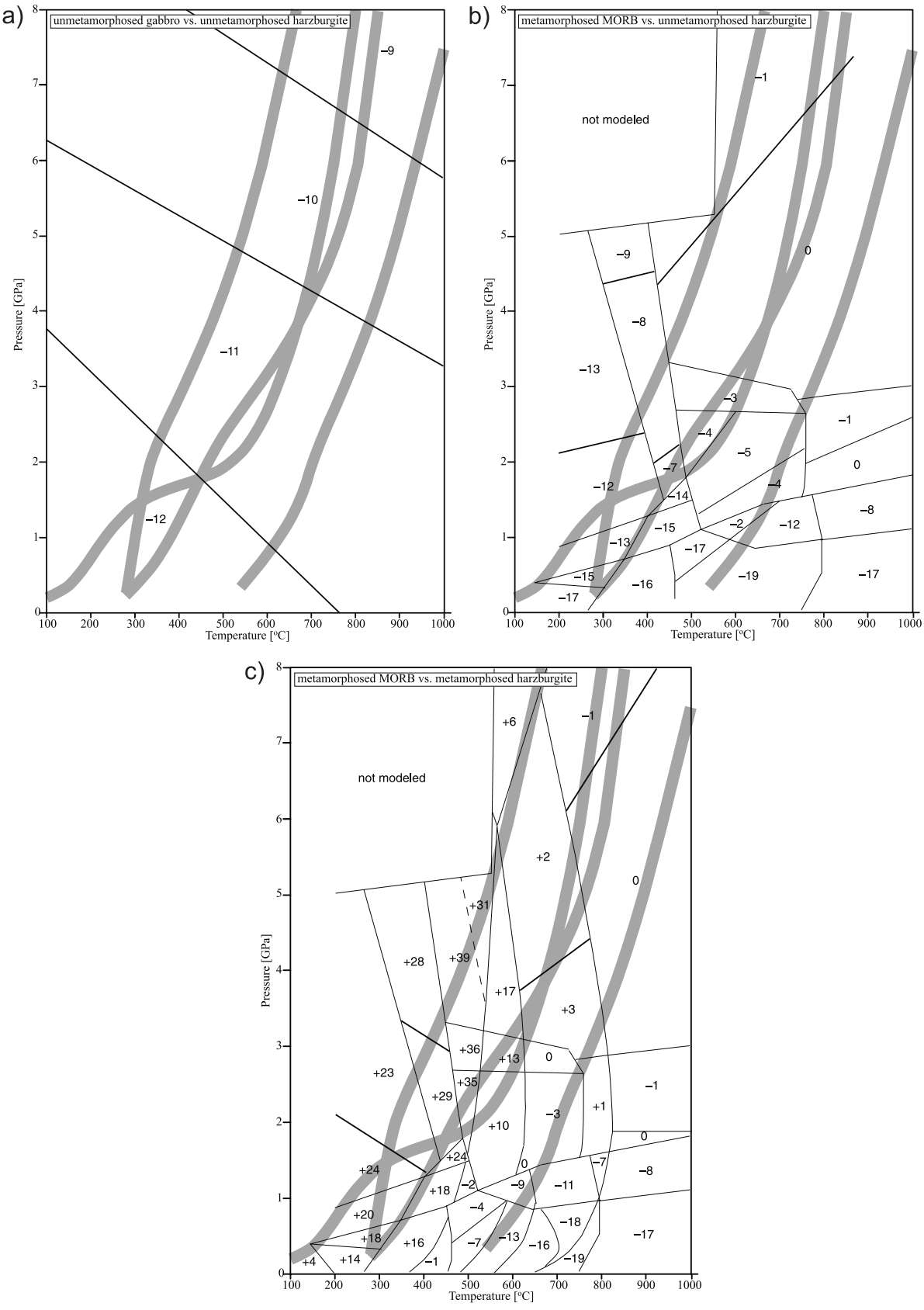
a)
unmetamorphosed gabbro vs. unmetamorphosed harzburgite
−9
−10
−11
−12
Pressure [GPa]
Temperature [°C]
b)
metamorphosed MORB vs. unmetamorphosed harzburgite
not modeled
−1
−9
0
−8
−13
−3
−1
−4
−5
−7
0
−12
−4
−14
−8
−15
−2
−12
−13
−17
−15
−16
−19
−17
−17
Pressure [GPa]
Temperature [°C]
c)
metamorphosed MORB vs. metamorphosed harzburgite
not modeled
+6
−1
+2
0
+31
+28
+39
+17
+3
+36
+13
0
+23
+35
−1
+29
−3
+1
+10
0
+24
0
−7
−8
+24
+18
−2
−9
−11
+20
−4
−18
+18
+16
−7
−13
−16
−17
+4
+14
−1
−19
Pressure [GPa]
Temperature [°C]

Table 8. Tohoku at 4 GPa (~125 km)[a]

Lithology	Figure	V_P	V_S	V_P/V_P Dry,[b]	V_S/V_S Dry[b]	V_P/V_P Wet[c]	V_S/V_S Wet[c]
laE	8a	7.87	4.36	−9%	−10%	+29%	+56%
Metastable dry gabbro	7b	7.66	4.22	−11%	−13%	+26%	+51%
Dry MORB	7a	7.58	4.15	−12%	−15%	+24%	+48%
Dry spinel harzburgite	11	8.63	4.86	0%	0%	+41%	+74%
Fully hydrated lherzolite	9	6.42	3.16	−26%	−35%	+5%	+13%
Fully hydrated harzburgite	12	6.10	2.80	−29%	−42%	0%	0%
Serpentinite	13	6.05	2.68	−30%	−45%	−1%	−4%
Low-velocity layer observations				V_P/V_P(mantle)	V_S/V_S(mantle)		
Matsuzawa et al. [1986]				−6%/−12%			
Abers [2000]				−6 + 2%	−4 + 2%		

[a]From Figures 7, 8, 9, 10, 11, 12–13, calculated at Moho temperatures predicted by *Peacock and Wang* [1999]. V_P and V_S in km/s.
[b]Velocities relative to anhydrous harzburgite.
[c]Velocities relative to fully hydrated harzburgite. Compare with Figure 16.

at <60 km depth. From these velocities, they infer that the slab crust remains gabbroic and has not yet transformed to eclogite. This 60 km depth corresponds to our modeled [*Hacker et al.*, 2002] transformation from zoisite-bearing eclogite to eclogite. Using our thermal model of the Nankai subduction zone [*Hacker et al.*, 2003], at 40–60 km depth (~500°C), unaltered harzburgite should have V_P = 8.2 km/s, as observed. Our methodology predicts that unaltered gabbro at 40–60 km depth beneath Nankai should have V_P = 7.1–7.2 km/s, slightly faster than observed. If the crust is entirely altered to hydrous assemblages, it should have *P* wave speeds of 7.8–7.9 km/s (zoisite-amphibole eclogite) or 6.7 km/s (epidote blueschist) at these depths. Thus the observation of a slow waveguide to 40–60 km depth beneath Nankai is consistent with the presence of unaltered gabbro or blueschist, but not eclogite (Figure 16b).

8.3. Mantle Wedge Alteration

[32] As a final example, consider the reports of serpentinization of arc mantle wedges. *Graeber and Asch* [1999] found by tomographic inversion that the Nazca plate subducting beneath northern Chile is overlain at depths of 50–100 km by a layer with V_P/V_S ratios of 1.79 to >1.84. Examination of Figure 11b reinforces Graeber and Asch's conclusion that such ratios cannot represent unaltered mantle. Comparison of Figures 11b and 9b, 10, 12, and 13b shows, however, that such V_P/V_S ratios are easily explained by ~20% alteration to stable hydrous minerals.

[33] *Kamiya and Kobayashi* [2000] measured $V_P \sim 6.9$ km/s, $V_S \sim 3.4$ km/s, and Poisson's ratio is ~0.34 at depths of 20–45 km in a small region beneath central Japan. They concluded from the data of *Christensen* [1972] that these observations are consistent with 50 vol % serpentinized peridotite. Our calculations indicate higher fractions of hydrous minerals, 60–80%, but reinforce the general conclusion that mantle wedges are locally hydrated.

9. Conclusions

[34] Our model produces calculated physical properties of MORB, lherzolite, harzburgite, and serpentinite in subduction zones using a compilation of mineral physical property measurements, a new set of phase diagrams, and subduction zone thermal models. These data are used to calculate H_2O content, density and seismic wave speeds of subduction zone rocks. New insights are provided into (1) the presence of hydrous phases and the distribution of H_2O within a subduction zone; (2) the densification of the subducting slab and resultant effects on measured gravity and slab shape; and (3) the variations in seismic wave speeds resulting from thermal and metamorphic processes at depth.

Appendix A: Calculation Method

[35] We calculated the physical properties of minerals at elevated pressure and temperature via the following algo-

Figure 16. (opposite) Percent differences in velocities between pairs of rocks. Metamorphic facies boundaries as in Figures 1 and 4; gray lines show P–T paths for Moho of Tohoku, Nankai, Costa Rica, and Cascadia subduction zones. (a) V_P in unmetamorphosed gabbro relative to V_P in unmetamorphosed harzburgite; gabbro is 9–12% slower. (b) V_P in metamorphosed, fully hydrated MORB relative to V_P in unmetamorphosed harzburgite; metamorphosed MORB ranges from significantly slower (at low P or low T) to indistinguishable from unmetamorphosed harzburgite at eclogite-facies conditions. (c) V_P in metamorphosed, fully hydrated MORB relative to V_P in metamorphosed, fully hydrated harzburgite; the presence of hydrous minerals in harzburgite means that at low P and high T, metaharzburgite is faster than meta-MORB, and at low T, this situation is reversed. (d) V_P in metamorphosed, hydrated MORB relative to V_P in unmetamorphosed MORB and V_P/V_S in metamorphosed, hydrated MORB relative to V_P/V_S in unmetamorphosed MORB. Metamorphism of MORB changes V_P/V_S insignificantly. (e) V_P in metamorphosed, hydrated harzburgite relative to V_P in unmetamorphosed harzburgite, and V_P/V_S in metamorphosed hydrated harzburgite relative to V_P/V_S in unmetamorphosed harzburgite. Metamorphism of harzburgite produces large changes in V_P/V_S due to formation of serpentine, making it a good measure of mantle hydration.

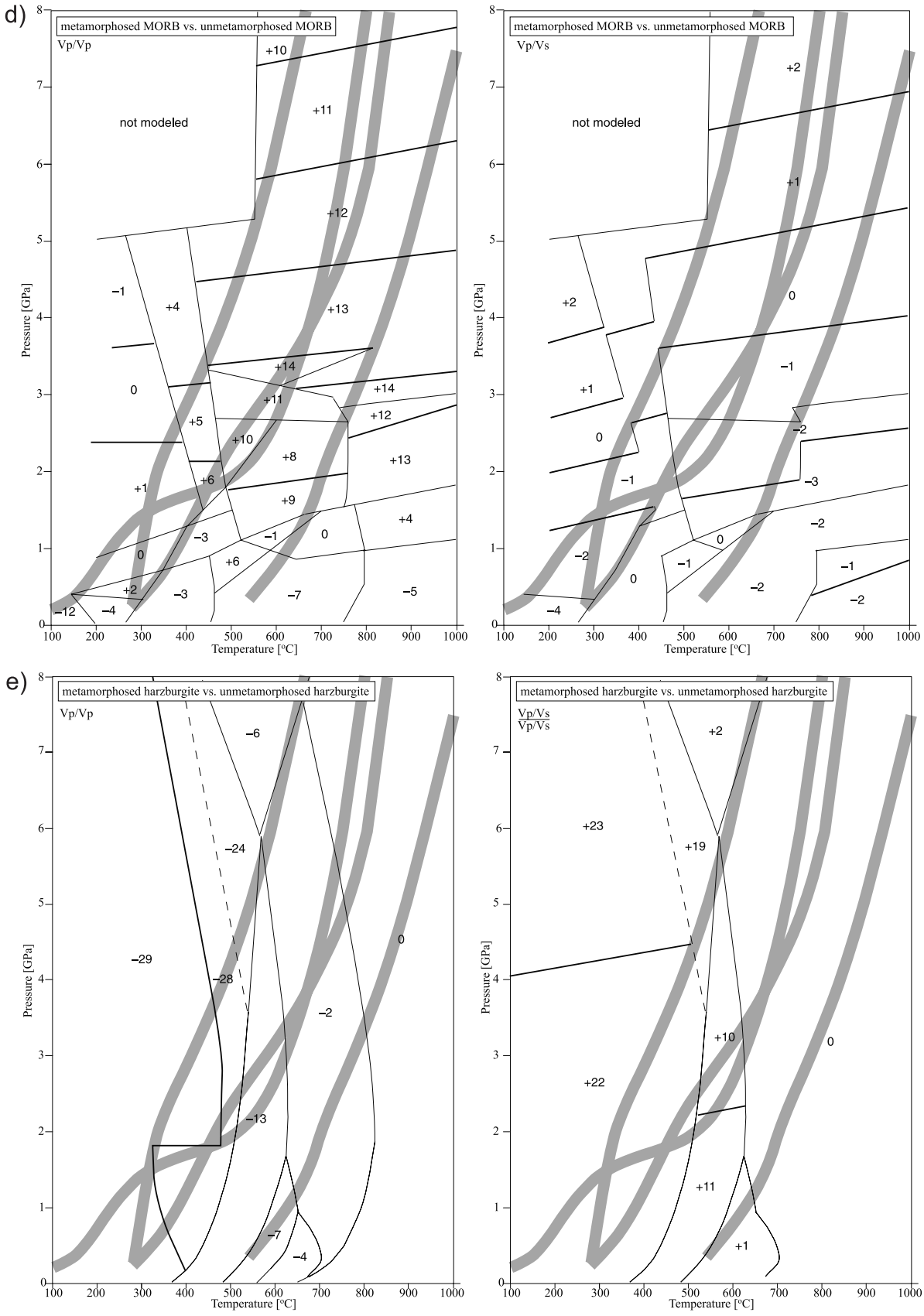

Figure 16. (continued)

rithm, based on *Bina and Helffrich* [1992]. *Holland and Powell* [1998] advocated a relationship between expansivity α and temperature $T(K)$, defined by a single constant a° for each mineral:

$$\alpha(T) = a^\circ\left(1 - 10\sqrt{T}\right),$$

which gives

$$\partial\alpha/\partial T = 5a^o/T^{3/2}$$

$$\Phi \equiv \ln(V(T)/V_o) = \int_{T_o}^{T} \alpha(T)dT = a^o\left\{(T - T_o) - 20\left(\sqrt{T} - \sqrt{T_o}\right)\right\},$$

where $V(T)$ is the molar volume at temperature, V_o is the molar volume at STP, and T_o = 298 K.

[36] The density at elevated temperature $\rho(T)$ is related to the density at STP ρ_o by

$$\rho(T) = \rho_o e^{-\Phi}.$$

[37] The isothermal bulk modulus at elevated temperature $K_T(T)$ is related to the isothermal bulk modulus at STP by

$$K_T(T) = K_{T_o} e^{-\delta_T \Phi}$$

where δ_T is the second Grüneisen parameter. The shear modulus at elevated temperature $\mu(T)$ follows in similar fashion from the shear modulus at STP:

$$\mu_T(T) = \mu_{T_o} e^{-\Gamma\Phi},$$

where

$$\Gamma = (\partial \ln\mu/\partial \ln\rho)_P = -(1/\mu\alpha)(\partial\mu/\partial T).$$

[38] The finite strain f is calculated recursively from

$$P/K_T = 3f(1+2f)^{5/2} \cdot\left\{1 - 2\zeta f + f^2/6[4\zeta(4 - 3K') + 5(3K' - 5)]\right\}$$

where

$$\zeta = 0.75(4 - K')$$
$$K' = (dK_T/dP)_T$$

typically evaluated at T_o (K'_T in Table 1). The density at elevated pressure $\rho(P)$ is then

$$\rho(P) = \rho_o(1+2f)^{3/2}.$$

[39] The bulk modulus at elevated pressure and temperature $K_T(T,P)$ is

$$K_T(T,P) = K_T(T)\left\{1 - (5 - 3K')f^2(3K' - 7)(3K' - 5)\right\} \cdot(1+2f)^{5/2}$$

[40] The expansivity at elevated pressure and temperature $\alpha(T,P)$ is

$$\alpha(T,P) = \alpha(T)[\rho(P)/\rho_o]^{-\delta_T}.$$

[41] The isentropic bulk modulus K_S is

$$K_S = K_T(T,P)[1 + T\gamma_{th}\alpha(T,P)],$$

where γ_{th} is the first Grüneisen parameter. The shear modulus at elevated pressure and temperature $\mu(T,P)$ is

$$\mu(T,P) = \mu(T)(1+2f)^{5/2}\{1 - f[5 - 3\mu' K_T(T)/\mu(T)] + 0.5f^2[9(K' - 4)\mu' K_T(T)/\mu(T) + 35]\}.$$

[42] The density at elevated pressure and temperature $\rho(P,T)$ is

$$\rho(T,P) = [\rho(P)/\rho_o]\rho(T)$$

from which the P wave velocity V_P, shear wave velocity V_S, and Poisson's ratio ν can be calculated:

$$V_P = \sqrt{K_S + 4/3\mu/\rho},$$
$$V_S = \sqrt{\mu/\rho},$$
$$\nu = (3K_S - 2\mu)/(6K_S + 2\mu).$$

[43] The physical property Ψ of a mineral aggregate is then calculated from the physical property Ψ_i of n constituent minerals using a Voigt-Reuss-Hill average:

$$\Psi = \{\Psi_{V+}\Psi_R\}/2 = \left\{\left(\sum_{i=1}^{n}\Psi_i\nu_i\right)/n + \left(1/\sum_{i=1}^{n}[\nu_i/\Psi_i]\right)/n\right\}/2,$$

where ν_i is the volume proportion of each mineral and the first and second terms are Ψ_V, the Voigt bounds, and Ψ_R, the Reuss bounds. Because mass in aggregates is a simple sum of component masses, only Ψ_V is used in calculating ρ for aggregates.

[44] **Acknowledgments.** Supported by grants from the National Science Foundation. Thoughtfully reviewed by W.G. Ernst and two anonymous reviewers. Ross Angel and Nancy Ross provided preprints and helpful reviews of our mineral physical parameter compilation. Stephan Husen provided sundry seismology tutorials to B.R.H.

References

Abers, G. A., Hydrated subducted crust at 100–250 km depth, *Earth Planet. Sci. Lett.*, *176*, 323–330, 2000.

Alexandrov, K. S., and T. V. Ryzhova, Elastic properties of rock-forming minerals, 1, pyroxenes and amphiboles, *Bull. Acad. Sci. USSR, Geophys. Ser.*, *9*, 1165–1168, 1961.

Alt, J. C., et al., *Proceedings of the Ocean Drilling Program, Initial Reports*, vol. 148, Ocean Drill. Program, College Station, Tex., 1993.

Anderson, D. L., *Theory of the Earth*, 366 pp., Blackwell Sci., Malden, Mass., 1989.

Anderson, O. L. and D. G. Isaak, Elastic constants of mantle minerals at high temperature, in *Mineral Physics and Crystallography: A Handbook of Physical Constants*, *AGU Ref. Shelf*, vol. 2, edited by T. J. Ahrens, pp. 64–97, AGU, Washington, D. C., 1995.

Anderson, O., D. Isaak, and H. Oda, High-temperature elastic constant data on minerals relevant to geophysics, *Rev. Geophys.*, *30*, 57–90, 1992.

Angel, R. J., R. M. Hazen, T. C. McCormick, C. T. Prewitt, and J. R. Smyth, Comparative compressibility of end-member feldspars, *Phys. Chem.f Miner.*, *15*, 513–518, 1988.

Ayuso, R. A., A. E. Bence, and S. R. Taylor, Upper Jurassic tholeiitic basalts from DSDP Leg 11, *J. Geophys. Res.*, *81*, 4305–4325, 1976.

Bailey, E., and J. R. Holloway, Experimental determination of elastic properties of talc to 800°C, 0.5 GPa: Calculations of the effect on hydrated peridotite, and implications for cold subduction zones, *Earth Planet. Sci. Lett.*, *183*, 487–498, 2000.

Bass, J. D., Elasticity of minerals, glasses, and melts, in *Mineral Physics and Crystallography: A Handbook of Physical Constants*, *AGU Ref. Shelf*, vol. 2, edited by T. J. Ahrens, pp. 45–63, AGU, Washington, D. C., 1995.

Bina, C. R., and G. R. Helffrich, Calculation of elastic properties from thermodynamic equation of state principles, *Annu. Rev. Earth Planet. Sci.*, *20*, 527–552, 1992.

Bose, K., and A. Navrotsky, Thermochemistry and phase equilibria of hydrous phases in the system MgO-SiO_2-H_2O: Implications for volatile transport to the mantle, *J. Geophys. Res.*, *103*, 9713–9719, 1998.

Boyle, A. P., Metamorphism of basic and pelitic rocks at Sulitjelma, Norway, *Lithos*, *19*, 113–128, 1986.

Browning, P., Cryptic variation within the cumulate sequence of the Oman ophiolite: Magma chamber depth and petrological implications, in *Ophiolites and Oceanic Lithosphere*, edited by I. G. Gass, S. J. Lippard, and A. W. Shelton, *Geol. Soc. Spec. Publ., 13*, 71–82, 1984.

Cann, J. R., Basalts from the ocean floor, in *The Oceanic Lithosphere*, edited by C. Emiliani, pp. 363–390, John Wiley, New York, 1981.

Carlson, R. L., The abundance of ultramafic rocks in Atlantic Ocean crust, *Geophys. J. Int.*, *144*, 37–48, 2001.

Caron, J.-M., and G. Pequignot, The transition between blueschists and lawsonite-bearing eclogites based on observations from Corsican metabasalts, *Lithos*, *19*, 205–218, 1986.

Carswell, D. A., M. A. Harvey, and A. Al-Samman, The petrogenesis of contrasting Fe-Ti and Mg-Cr garnet peridotite types in the high grade gneiss complex of western Norway, *Bull. Mineral.*, *106*, 727–750, 1983.

Chinnery, N., A. R. Pawley, and S. M. Clark, The equation of state of lawsonite to 7 GPa and 873 K, and calculation of its high pressure stability, *Am. Mineral.*, *85*, 1001–1008, 2000.

Christensen, N. I., The abundance of serpentinites in the oceanic crust, *J. Geol.*, *80*, 709–719, 1972.

Christensen, N. I., Compressional wave velocities in possible mantle rocks to pressures of 30 kilobars, *J. Geophys. Res.*, *79*, 407–412, 1974.

Christensen, N. I., Seismic velocities, in *Handbook of Physical Properties of Rocks*, edited by R. S. Carmichael, pp. 1–228, CRC Press, Boca Raton, Fla., 1982.

Christensen, N. I., Poisson's ratio and crustal seismology, *J. Geophys. Res.*, *101*, 3139–3156, 1996.

Christensen, N. I., and W. D. Mooney, Seismic velocity structure and composition of the continental crust: A global view, *J. Geophys. Res.*, *100*, 9761–9788, 1995.

Coleman, R. G., *Ophiolites: Ancient Oceanic Lithosphere?*, Springer-Verlag, New York, 1977.

Coleman, R. G., D. E. Lee, L. B. Beatty, and W. W. Brannock, Eclogites and eclogites: Their differences and similarities, *Geol. Soc. Am. Bull.*, *76*, 483–508, 1965.

Comodi, P., and P. F. Zanazzi, High-pressure behavior of clinozoisite and zoisite: An x-ray diffraction study, *Am. Mineral.*, *82*, 452–459, 1997.

Comodi, P., M. Mellini, L. Ungaretti, and P. F. Zanazzi, Compressibility and high-pressure structure refinement of tremolite, pargasite and glaucophane, *Eur. J. Mineral.*, *3*, 485–499, 1991.

Comodi, P., P. F. Zanazzi, S. Poli, and M. W. Schmidt, High-pressure behavior of kyanite: Compressibility and structural deformation, *Am. Mineral.*, *82*, 452–459, 1997.

Cotkin, S. J., Conditions of metamorphism in an Early Paleozoic blueschist: Schist of Skookum Gulch, northern California, *Contrib. Mineral. Petrol.*, *96*, 192–200, 1987.

Davies, H. L., and R. G. Warren, Eclogites of the D'Entrecasteaux Islands, *Contrib. Mineral. Petrol.*, *112*, 463–474, 1992.

Davies, J. H., Simple analytical model for subduction zone thermal structures, *Geophys. J. Int.*, *139*, 823–828, 1999.

Dick, H. J. B., P. S. Meyer, S. H. Bloomer, S. H. Kirby, D. S. Stakes, and C. Mawer, Lithostratigraphic evolution of an in-situ section of oceanic layer 3, *Proc. Ocean Drill. Program Sci. Results*, *118*, 439–538, 1991.

Dick, H. J. B., et al., A long in situ section of the lower ocean crust: Results of ODP Leg 176 drilling at the Southwest Indian Ridge, *Earth Planet. Sci. Lett.*, *179*, 31–51, 2000.

Dilek, Y., E. M. Moores, and H. Furnes, Structure of modern oceanic crust and ophiolites and implications for faulting and magmatism at oceanic spreading centers, in *Faulting and Magmatism at Mid-Ocean Ridges*, *Geophys. Monogr. Ser.*, vol. 106, edited by W. R. Buck et al., pp. 219–265, AGU, Washington, D. C., 1998.

El-Shazly, A. K., Petrology of lawsonite-, pumpellyite- and sodic-amphibole bearing metabasites from northeast Oman, *J. Metamorph. Geol.*, *12*, 23–48, 1994.

El-Shazly, A. E.-D., R. G. Coleman, and J. G. Liou, Eclogites and blueschists from northeastern Oman: Petrology and P–T evolution, *J. Petrol.*, *31*, 629–666, 1990.

El-Shazly, A. K., M. A. Worthing, and J. G. Liou, Interlayered eclogites, blueschists and epidote amphibolites from NE Oman: A record of protolith compositional control and limited fluid infiltration, *J. Petrol.*, *38*, 1461–1487, 1997.

Elthon, D., Petrology of gabbroic rocks from the Mid-Cayman Rise spreading center, *J. Geophys. Res.*, *92*, 658–682, 1987.

Erdmer, P., and H. Helmstaedt, Eclogite from central Yukon: A record of subduction at the western margin of ancient North America, *Can. J. Earth Sci.*, *20*, 1389–1408, 1983.

Ernst, W. G., Mineralogic study of eclogitic rocks from Alpe Arami, Lepontine Alps, southern Switzerland, *J. Petrol.*, *18*, 371–398, 1977.

Evans, B. W., V. Trommsdorff, and W. Richter, Petrology of an eclogite-metarodingite suite at Cima di Gagnone, Ticino, Switzerland, *Am. Mineral.*, *64*, 15–31, 1979.

Evans, B. W., V. Trommsdorff, and G. G. Goles, Geochemistry of high-grade eclogites and metarodingites from the central Alps, *Contrib. Mineral. Petrol.*, *76*, 301–311, 1981.

Fei, Y., Thermal expansion, in *Mineral Physics and Crystallography: A Handbook of Physical Constants*, vol. 2, edited by T. J. Ahrens, pp. 29–44, AGU, Washington, D. C., 1995.

Furlong, K. P., and D. M. Fountain, Continental crustal underplating: Thermal considerations and seismic-petrologic consequences, *J. Geophys. Res.*, *91*, 8285–8294, 1986.

Ghent, E. D., M. Z. Stout, and P. Erdmer, Pressure-temperature evolution of lawsonite-bearing eclogites, Pinchi Lake, British Columbia, *J. Metamorph. Geol.*, *11*, 279–290, 1993.

Glassley, W. E., and K. Sørensen, Constant Ps-T amphibolite to granulite facies transition in Agto (West Greenland) metadolerites: Implications and applications, *J. Petrol.*, *21*, 69–105, 1980.

Godard, G., Petrology of some eclogites in the Hercynides: The eclogites from the southern Armorican Massif, France, in *Eclogites and Eclogite-Facies Rocks*, edited by D. C. Smith, pp. 451–519, Elsevier Sci., New York, 1988.

Graeber, F., and G. Asch, Three-dimensional models of *P* wave velocity and *P*-to-*S* velocity ratio in the southern central Andes by simultaneous inversion of local earthquake data, *J. Geophys. Res.*, *104*, 20,237–20,256, 1999.

Grevel, K.-D., E. U. Nowlan, D. W. Fasshauer, and M. Burchard, In situ X-ray diffraction investigation of lawsonite and zoisite at high pressures and temperatures, *Am. Mineral.*, *85*, 206–217, 2000.

Gubbins, D., and R. Sneider, Dispersion of P waves in subducted lithosphere: Evidence for an eclogite layer, *J. Geophys. Res.*, *96*, 6321–6333, 1991.

Hacker, B. R., Eclogite formation and the rheology, buoyancy, seismicity, and H_2O content of oceanic crust, in *Subduction: Top to Bottom*, *Geophys. Monogr. Ser.*, vol. 96, edited by G. E. Bebout et al., pp. 337–246, AGU, Washington, D. C., 1996.

Hacker, B. R., G. A. Abers, and S. M. Peacock, Theoretical mineralogy, density, seismic wave speeds, and H_2O content of the Cascadia subduction zone, with implications for intermediate-depth seismicity and earthquake hazard, *U. S. Geol. Surv. Open File Rep.*, *02-328*, 133–137, 2002.

Hacker, B. R., S. M. Peacock, and G. A. Abers, Subduction factory, 2, Intermediate-depth earthquakes in subducting slabs are linked to metamorphic dehydration reactions, *J. Geophys. Res.*, *108*, doi:10.1029/2001JB001129, in press, 2003.

Hazen, R. M., and L. W. Finger, The crystal structures and compressibilities of layer minerals at high pressure, II, Phlogopite and chlorite, *Am. Mineral.*, *63*, 293–296, 1978.

Helffrich, G., Subducted lithospheric slab velocity structure: Observations and mineralogical inferences, in *Subduction: Top to Bottom*, *Geophys. Monogr. Ser.*, vol. 96, edited by G. E. Bebout et al., pp. 215–222, AGU, Washington, D. C., 1996.

Helmstaedt, H. and D. J. Schulze, Eclogite-facies ultramafic xenoliths from Colorado Plateau diatreme breccias: Comparison with eclogites in crustal environments, evaluation of the subduction hypothesis, and implications for eclogite xenoliths from diamondiferous kimberlites, in *Eclogites and Eclogite-Facies Rocks*, edited by D. C. Smith, pp. 387–450, Elsevier Sci., New York, 1988.

Hill, R., The elastic behavior of crystalline aggregates, *Philos. Trans. R. Soc. London, Ser. A*, *65*, 349–354, 1952.

Holland, T. J. B., and R. Powell, An internally consistent thermodynamic data set for phases of petrological interest, *J. Metamorph. Geol.*, *16*, 309–343, 1998.

Hori, S., Seismic waves guided by untransformed oceanic crust subducted into the mantle: The case of the Kanto district, central, Japan, *Tectonophysics*, *176*, 355–376, 1990.

Iidaka, T., and M. Mizoue, *P*-wave velocity structure inside the subducting Pacific Plate beneath the Japan region, *Phys. Earth Planet. Inter.*, *66*, 203–213, 1991.

Jackson, J. M., S. V. Sinogeikin, and J. D. Bass, Elasticity of $MgSiO_3$ orthoenstatite, *Am. Mineral.*, *84*, 677–680, 1999.

Kamiya, S., and Y. Kobayashi, Seismological evidence for the existence of serpentinized wedge mantle, *Geophys. Res. Lett.*, *27*, 819–822, 2000.

Karson, J., Internal structure of oceanic lithosphere: A perspective from tectonic windows, in *Faulting and Magmatism at Mid-Ocean Ridges*, *Geophys. Monogr. Ser.*, vol. 106, edited by W. R. Buck et al., pp. 177–217, AGU, Washington, D. C., 1998.

Kern, H., S. Gao, Z.-M. Jin, T. Popp, and S. Jin, Petrophysical studies on rocks from the Dabie ultrahigh-pressure (UHP) metamorphic belt, central China: Implications for the composition and delamination of the lower crust, *Tectonophysics*, *301*, 191–215, 1999.

Kerrick, D. M., and J. A. D. Connolly, Metamorphic devolatilization of subducted oceanic metabasalts: Implications for seismicity, arc magmatism and volatile recycling, *Earth Planet. Sci. Lett.*, *189*, 19–29, 2001.

Knittle, E., Static compression measurements of equations of state, in *Mineral Physics and Crystallography: A Handbook of Physical Constants*, *AGU Ref. Shelf*, vol. 2, edited by T. J. Ahrens, pp. 98–142, AGU, Washington, D. C., 1995.

Laird, J., and A. L. Albee, High-pressure metamorphism in mafic schist from northern Vermont, *Am. J. Sci.*, *281*, 97–126, 1981.

Levien, L., C. T. Prewitt, and D. J. Weidner, Structure and elastic properties of quartz at pressure, *Am. Mineral.*, *65*, 920–930, 1980.

Liou, J. G., and R. Y. Zhang, Petrogenesis of an ultrahigh-pressure garnet-bearing ultramafic body from Maowu, Dabie Mountains, east-central China, *Island Arc*, *7*, 115–134, 1998.

Liou, J. G., C. O. Ho, and T. P. Yen, Petrology of some glaucophane schists and related rocks from Taiwan, *J. Petrol.*, *16*, 80–109, 1975.

Liou, J. G., B. R. Hacker, and R. Y. Zhang, Ultrahigh-pressure (UHP) metamorphism in the forbidden zone, *Science*, *287*, 1215–1216, 2000.

Lippard, S. J., A. W. Shelton, and I. G. Gass, *The Ophiolite of Northern Oman*, 178 pp., Geol. Soc. of London, London, 1986.

Luth, R. W., Is phase A relevant to the Earth's mantle?, *Geochim. Cosmochim. Acta*, *59*, 679–682, 1995.

Maresch, W. V., and K. Abraham, Petrography, mineralogy, and metamorphic evolution of an eclogite from the Island of Margarita, Venezuela, *J. Petrol.*, *22*, 337–362, 1981.

Matsuzawa, T., N. Umino, A. Hasegawa, and A. Takagi, Normal fault type events in the upper plane of the double-planed deep seismic zone beneath the northeastern Japan Arc, *J. Phys. Earth*, *34*, 85–94, 1986.

Mazzullo, L. J., and A. E. Bence, Abyssal tholeiites from DSDP leg 34: The Nazca Plate, *J. Geophys. Res.*, *81*, 4327–4351, 1976.

McDonough, W. F. and R. L. Rudnick, Mineralogy and composition of the upper mantle, in *Ultrahigh-Pressure Mineralogy*, *Rev. Mineral.*, vol. 37, edited by R. Hemley and H. K. Mao, pp. 139–164, Mineral. Soc. of Am., Washington, D. C., 1998.

Moore, T. E., Petrology and tectonic implications of the blueschist-bearing Puerto Nuevo melange complex, Vizcaino Peninsula, Baja California Sur, Mexico, in *Blueschists and Eclogites*, edited by B. W. Evans and E. H. Brown, *Mem. Geol. Soc. Am.*, *164*, 43–58, 1986.

Morgan, B., Petrology and mineralogy of eclogite and garnet amphibolite from Puerto Cabello, Venezuela, *J. Petrol.*, *11*, 101–145, 1970.

Mutter, C. Z., and J. C. Mutter, Variations in thickness of layer 3 dominate oceanic crustal structure, *Earth Planet. Sci. Lett.*, *117*, 295–317, 1993.

Ohno, I., Temperature variation of elastic properties of a-quartz up to the a-b transition, *J. Phys. Earth*, *43*, 157–169, 1995.

Okamoto, K., and S. Maruyama, The high-pressure synthesis of lawsonite in the MORB + H_2O system, *Am. Mineral.*, *84*, 362–373, 1999.

Okay, A. I., Lawsonite zone blueschists and a sodic amphibole producing reaction in the Tavansli region, northwest Turkey, *Contrib. Mineral. Petrol.*, *75*, 179–186, 1980a.

Okay, A. I., Mineralogy, petrology and phase relations of glaucophane-lawsonite zone blueschists from the Tavansli region, northwest Turkey, *Contrib. Mineral. Petrol.*, *72*, 243–255, 1980b.

Okay, A. I., Paragonite eclogites from Dabie Shan, China: Re-equilibration during exhumation?, *J. Metamorph. Geol.*, *13*, 449–460, 1995.

Ota, T., M. Terabayashi, C. D. Parkinson, and H. Masago, Thermobaric structure of the Kokchetav ultrahigh-pressure-high-pressure massif deduced from a north-south transect in the Kulet and Saldat-Kol regions, northern Kazakhstan, *Island Arc*, *9*, 328–357, 2000.

Pawley, A., Stability of clinohumite in the system MgO-SiO_2-H_2O, *Contrib. Mineral. Petrol.*, *138*, 284–291, 2000.

Pawley, A. R., and J. R. Holloway, Water sources for subduction zone volcanism: New experimental constraints, *Science*, *260*, 664–667, 1993.

Pawley, A. R., and B. J. Wood, The low-pressure stability of phase A, $Mg_7Si_2O_8(OH)_6$, *Contrib. Mineral. Petrol.*, *124*, 90–97, 1996.

Pawley, A. R., S. A. T. Redfern, and B. J. Wood, Thermal expansivities and compressibilities of hydrous phases in the system MgO-SiO_2-H_2O: Talc, phase A, 10-Å phase, *Contrib. Mineral. Petrol.*, *122*, 301–307, 1995.

Pawley, A., S. A. T. Redfern, and T. J. B. Holland, Volume behavior of hydrous minerals at high pressure and temperature, I, Thermal expansion of lawsonite, zoisite, clinozoisite, and diaspore, *Am. Mineral.*, *81*, 335–340, 1996.

Pawley, A., N. J. Chinnery, and S. M. Clark, Volume measurements of zoisite and simultaneously elevated pressure and temperature, *Am. Mineral.*, *83*, 1030–1036, 1998.

Peacock, S. M., Creation and preservation of subduction-related inverted metamorphic gradients, *J. Geophys. Res.*, *92*, 12,763–12,781, 1987.

Peacock, S. M., Numerical simulation of metamorphic pressure-temperature-time paths and fluid production in subducting slabs, *Tectonics*, *9*, 1197–1211, 1990.

Peacock, S. M., and K. Wang, Seismic consequences of warm versus cool subduction metamorphism: Examples from southwest and northeast Japan, *Science*, *286*, 937–939, 1999.

Pearce, J. A., Statistical analysis of major element patterns in basalts, *J. Petrol.*, *17*, 15–43, 1976.

Perfit, M. R., and D. J. Fornari, Geochemical studies of abyssal lavas recovered by DSRV Alvin from eastern Galapagos Rift, Inca Transform, and Ecuador Rift, 2, Phase chemistry and crystallization history, *J. Geophys. Res.*, *88*, 10,530–10,550, 1983.

Poli, S., and M. W. Schmidt, The high-pressure stability of hydrous phases in orogenic belts: An experimental approach on eclogite-forming processes, *Tectonophysics*, *273*, 169–184, 1997.

Powell, R., T. Holland, and B. Worley, Calculating phase diagrams involving solid solutions via non-linear equations, with examples using THERMOCALC, *J. Metamorph. Geol.*, *16*, 577–588, 1998.

Preto, V. A. G., Amphibolites from the Grand Forks Quadrangle of British Columbia, Canada, *Geol. Soc. Am. Bull.*, *81*, 763–782, 1970.

Redfern, S. A. T., and R. J. Angel, High-pressure behaviour and equation of state of calcite, $CaCO_3$, *Contrib. Mineral. Petrol.*, *134*, 102–106, 1999.

Reid, A. M., R. W. Brown, J. B. Dawson, G. G. Whitfield, and J. C. Siebert, Garnet and pyroxene compositions in some diamondiferous eclogites, *Contrib. Mineral. Petrol.*, *58*, 203–220, 1976.

Robinson, P. T., et al., *Proceedings of the Ocean Drilling Program*, *Initial Reports*, vol. 118, Ocean Drill. Program, College Station, Tex., 1989.

Rogers, G. C., Earthquakes and earthquake hazards in the Vancouver area, *Bull. Geol. Surv. Can.*, *525*, 17–25, 1998.

Royden, L. H., The steady state thermal structure of eroding orogenic belts and accretionary prisms, *J. Geophys. Res.*, *98*, 4487–4507, 1993.

Ryzhova, T. V., Elastic properties of plagioclase, *Bull. Acad. Sci. USSR, Geophys. Ser.*, *7*, 633–635, 1964.

Sclater, J. G., C. Jaupart, and D. Galson, The heat flow through oceanic and continental crust and the heat loss of the Earth, *Rev. Geophys.*, *18*, 269–311, 1980.

Shearer, P. M., and J. A. Orcutt, Compressional and shear wave anisotropy in the oceanic lithosphere—The Ngendei seismic refraction experiment, *Geophys. J. R. Astron. Soc.*, *53*, 259–288, 1986.

Sinogeikin, S. V., and J. D. Bass, Single-crystal elasticity of pyrope and MgO to 20 GPa by Brillouin scattering in the diamond cell, *Phys. Earth Planet. Inter.*, *120*, 43–62, 2000.

Smyth, J. R. and T. C. McCormick, Crystallographic data for minerals, in *Mineral Physics and Crystallography: A Handbook of Physical Constants*, *AGU Ref. Shelf*, vol. 2, edited by T. J. Ahrens, pp. 1–17, AGU, Washington, D. C., 1995.

Staudigal, H., T. Plank, B. White, and H.-R. Schminke, Geochemical fluxes during seafloor alteration of the basaltic upper oceanic crust: DSDP Sites 417 and 418, in *Subduction: Top to Bottom*, *Geophys. Monogr. Ser.*, vol. 96, edited by G. E. Bebout et al., pp. 19–37, AGU, Washington, D. C., 1996.

Stephenson, N. C. N., and H. D. Hensel, Amphibolites and related rocks from the Wongwibinda metamorphic complex, northern N.S.W., Australia, *Lithos*, *15*, 59–75, 1982.

Thelin, P., M. Sartori, R. Lengeler, and J. P. Scharer, Eclogites of Paleozoic or early Alpine age in the basement of the Penninic Siviez-Mischabel nappe, Wallis, Switzerland, *Lithos*, *25*, 71–88, 1990.

Tiezzi, L. J., and R. B. Scott, Crystal fractionation in a cumulate gabbro, Mid-Atlantic Ridge, 26°N, *J. Geophys. Res.*, *85*, 5438–5454, 1980.

Toksöz, M. N., J. W. Minear, and B. R. Julian, Temperature field and geophysical effects of a downgoing slab, *J. Geophys. Res.*, *76*, 1113–1138, 1971.

Tyburczy, J. A., Shock wave equation of state of serpentine to 150 GPa: Implications for the occurrence of water in the Earth's lower mantle, *J. Geophys. Res.*, *96*, 18,011–18,027, 1991.

Ulmer, P., and V. Trommsdorff, Serpentine stability related to mantle depths and subduction-related magmatism, *Science*, *268*, 858–861, 1995.

van der Hilst, R. D., and R. Snieder, High-frequency precursors to P wave arrivals in New Zealand: Implications for slab structure, *J. Geophys. Res.*, *101*, 8473–8488, 1996.

Vielzeuf, D., and M. W. Schmidt, Melting relations in hydrous systems revisited: Application to metapelites, metagraywackes and metabasalts, *Contrib. Mineral. Petrol.*, *141*, 251–267, 2001.

Wang, Z., and S. Ji, Elasticity of six polycrystalline silicate garnets at pressure up to 3.0 GPa, *Am. Mineral.*, *86*, 1209–1218, 2001.

Welch, M. D., and W. G. Marshall, High-pressure behavior of clinochlore, *Am. Mineral.*, *86*, 1380–1386, 2001.

White, R. S., D. McKenzie, and R. K. O'Nions, Oceanic crustal thickness from seismic measurements and rare earth element inversions, *J. Geophys. Res.*, *97*, 19,683–19,715, 1992.

Wilson, M., *Igneous Petrogenesis*, 466 pp., Unwin Hyman, Boston, Mass., 1989.

Wunder, B., Equilibrium experiments in the system MgO-SiO_2-H_2O (MSH); stability fields of clinohumite-OH [$Mg_9Si_4O_{16}(OH)_2$], chondrodite-OH ([$Mg_5Si_2O_8(OH)_2$] and phase A ($Mg_7Si_2O_8(OH)_6$), *Contrib. Mineral. Petrol.*, *132*, 111–120, 1998.

Wunder, B., and W. Schreyer, Antigorite: High-pressure stability in the system MgO-SiO_2-H_2O (MSH), *Lithos*, *41*, 213–227, 1997.

Zhang, R., T. Hirajima, S. Banno, B. Cong, and J. G. Liou, Petrology of ultrahigh-pressure rocks from the southern Su-Lu region, eastern China, *J. Metamorph. Geol.*, *13*, 659–675, 1995.

G. A. Abers, Department of Earth Sciences, Boston University, Boston, MA 02215, USA. (abers@bu.edu)

B. R. Hacker, Department of Geological Sciences, University of California, Santa Barbara, CA 93106-9630, USA. (hacker@geology.ucsb.edu)

S. M. Peacock, Department of Geological Sciences, Arizona State University, Tempe, AZ 85287-1404, USA. (peacock@asu.edu)